Astral microtubule crosslinking by Feo safeguards uniform nuclear distribution in the *Drosophila* syncytium

Ojas Deshpande[*], Jorge de-Carvalho[*,#], Diana V. Vieira[*,#] and Ivo A. Telley[*,§]

[*] Instituto Gulbenkian de Ciência, Fundação Calouste Gulbenkian, Oeiras, Portugal

[#] Co-authors in alphabetical order

[§] Lead contact

Correspondence to: itelley@igc.gulbenkian.pt

Keywords: PRC1, Kif4, multinucleated cell, central spindle, microtubule interaction, nuclear positioning

Abstract:

The early insect embryo develops as a multinucleated cell distributing genome uniformly to the cell cortex. Mechanistic insight for nuclear positioning beyond cytoskeletal requirements is missing to date. Contemporary hypotheses propose actomyosin driven cytoplasmic movement transporting nuclei, or repulsion of neighbor nuclei driven by microtubule motors. Here, we show that microtubule crosslinking by Feo and Klp3A is essential for nuclear distribution and internuclear distance maintenance. Germline knockdown causes irregular, less dense nuclear delivery to the cell cortex and smaller distribution in *ex vivo* embryo explants. A minimal internuclear distance is maintained in explants from control embryos but not from Feo-depleted embryos, following micromanipulation assisted repositioning. A dimerization deficient Feo abolishes nuclear separation in embryo explants while the full-length protein rescues the genetic knockdown. We conclude that Feo and Klp3A crosslinking of antiparallel microtubule overlap generates a length-regulated mechanical link between neighboring microtubule asters. Enabled by a novel experimental approach, our study illuminates an essential process of embryonic multicellularity.

Introduction

The nucleus relocates within the cell boundary in response to cell function (Bone and Starr, 2016; Gundersen and Worman, 2013). Aberrant nuclear positioning has been linked to failure of fundamental processes such as early embryo development, cell differentiation, cell migration, polarity determination and homeostasis (Almonacid et al., 2015; 2019; Levy and Holzbaur, 2008; Minc et al., 2011; Neelam et al., 2015; Starr and Han, 2002). In mononuclear cells, cytoskeletal elements mechanically connect the nucleus to the cell cortex being the reference system for positioning (Dassow et al., 2009; Pecreaux et al., 2016). One exception are large eggs in which cytoskeletal links between the nucleus and the distant cell cortex are not achieved (Wühr et al., 2009). Conversely, a multinucleated cell – coenocyte – undergoing nuclear proliferation has to generate positional information to each additional nucleus and requires a mechanism that adjusts the distance between neighboring nuclei (Gibeaux et al., 2017; Manhart et al., 2018). The early embryo of *Drosophila melanogaster* is both large and multinucleated but exhibits a surprising positional regularity of hundreds of nuclei perturbed by cycles of meta-synchronous nuclear divisions (Foe and Alberts, 1983). During the first seven cycles, the nuclei spread axially from the anterior to the posterior end of the syncytial embryo and occupy the entire volume of the embryo(Baker et al., 1993). During nuclear cycles 7–9, most nuclei migrate to the embryo cortex, where they undergo additional rounds of division as they are anchored and prepared for cellularization (Lecuit and Wieschaus, 2000). Adequate number of nuclei and their proper positioning at the cortex determines cell size (Callaini et al., 1992) and precision of developmental patterning (Petkova et al., 2019), and is a result of regular distribution of ancestor nuclei during the preceding developmental phase (Kao and Megraw, 2009; Megraw et al., 1999; Vaizel-Ohayon and Schejter, 1999). The mechanisms required for maintaining uniform internuclear distances are not understood.

Drug inhibition and mutagenesis suggest that actomyosin mediated cortical contractions drive cytoplasmic streaming and transport the nuclei predominantly along the longer axis of the embryo (Callaini et al., 1992; Dassow and Schubiger, 1994; Deneke et al., 2019; Hatanaka and Okada, 1991; Royou et al., 2004; Wheatley et al., 1995). However, large-scale transport of cytoplasm does neither explain how a uniform distribution emerges nor how nuclei are kept separate. Conversely, astral microtubules from neighboring nuclei may interact and generate repulsive force by motor binding and sliding antiparallel overlaps (Baker et al., 1993), which is reminiscent of the spindle midzone model explaining spindle elongation during anaphase B (Fu et al., 2009; Khmelinskii et al., 2009; Scholey et al., 2016). The effector Klp61F, a homotetrameric, bipolar Kinesin-5 binds

58 two overlapping microtubules and, when microtubules are antiparallel, slides them outwards
59 reducing microtubule overlap length (Cheerambathur et al., 2013; Reinemann et al., 2017; Tao et
60 al., 2006). Fascetto (Feo) is the *Drosophila* homolog of the Ase1p/PRC1/MAP65 family of
61 homodimeric non-motor MAPs that preferentially binds antiparallel microtubule overlaps (Bieling
62 et al., 2010; Subramanian et al., 2010; Vernì et al., 2004). It accumulates at the spindle midzone
63 from anaphase to telophase upon cyclin B degradation and controls the binding affinity of
64 molecular motors in the spindle midzone (Hu et al., 2012; Khmelinskii et al., 2009; Kwon and
65 Scholey, 2004; Wang et al., 2015; Zhu et al., 2006). One of these motors is Klp3A, a Kinesin-4
66 homolog, an inhibitor of microtubule dynamics (Bieling et al., 2010; Bringmann et al., 2004;
67 Subramanian et al., 2013; Williams et al., 1997). PRC1 and Kinesin-4 are sufficient to form a stable
68 microtubule overlap *in vitro* (Bieling et al., 2010). Kinesin-5 can reduce overlapping, antiparallel
69 microtubules crosslinked by PRC1 *in vitro* (Subramanian et al., 2010), which was proposed to
70 contribute to force balance in the spindle midzone during anaphase B (Scholey et al., 2016).

71 Here, we investigated whether these three proteins are required for nuclear separation, lending
72 support to an aster–aster interaction model (Baker et al., 1993; Nguyen et al., 2014). We performed
73 a combination of gene knockdown, micromanipulation and perturbation by exogenous protein
74 addition in embryo explants which enable time-lapse visualization of nuclear and cytoskeletal
75 dynamics previously unachieved.

76 Results

77 *Feo localization confirms antiparallel microtubule overlaps between asters of non-sister nuclei*

78 Molecular crosslinking between astral microtubules of neighboring nuclei during the
79 preblastoderm embryo stage has largely been unexplored due to optical constraints in live imaging.
80 Using an extraction method to generate embryo explants from individual preblastoderm embryos
81 (de-Carvalho et al., 2018) expressing Klp61F::GFP and Feo::mCherry, and injected with
82 Alexa647-labeled Tubulin (Fig. 1A), we visualized the localization of Klp61F and Feo to infer
83 about their binding to spindle microtubules (Fig. 1B). Klp61F::GFP localized at the microtubule-
84 organizing centers, the metaphase spindle and the spindle midzone in anaphase, as described
85 previously for the nuclear divisions at the blastoderm stage (Cheerambathur et al., 2013; 2008;
86 Heck et al., 1993; Sharp et al., 1999; Tao et al., 2006) (Suppl. Video 1). Furthermore, during
87 anaphase B and telophase we observed Klp61F::GFP decorated microtubules intercalating with
88 those from the neighboring aster, raising the possibility of antiparallel alignment of these astral
89 microtubules, forming an overlap zone to which Kinesin-5 binds. On the other hand, Feo::mCherry

90 exhibited weak localization to the metaphase spindle but strong localization to the spindle midzone
91 during anaphase B and telophase (Fig. 1B, arrows), as previously described for blastoderm division
92 cycles (Wang et al., 2015). Strikingly, Feo also localized as small foci to the region between the
93 nuclei (Fig. 1B,C, arrowheads), thus reporting the presence of antiparallel microtubule overlaps to
94 which Feo binds with higher affinity than individual microtubules. *In vitro*, microtubule overlaps
95 that are decorated by Feo homologs are length controlled through the stabilization activity of
96 Kinesin-4 (Bieling et al., 2010). Thus, the signal of Feo along microtubule overlaps should have a
97 consistent length for a given concentration or activity of Feo and Klp3A. Thus, we measured the
98 length of Feo::mCherry signal foci during anaphase B (Fig. 1D). Because individual microtubules
99 were not resolved, we measured the orientation of the signal foci in the context of where
100 microtubules are growing and radially emanating from, the microtubule-organizing centers
101 (MTOC) at the spindle pole. In anaphase and telophase, the four nuclei emerging from any two
102 neighboring spindles define four MTOCs and, thus, four possible combinations of astral
103 microtubule interaction (Fig. 1C, right). We measured the angle θ between the long axes of the
104 signal foci and the closest connecting line between two MTOCs (Fig. 1E). θ deviated little from
105 zero, supporting the notion that Feo reports microtubule overlaps along the shortest path between
106 neighboring asters. Altogether, in explants from preblastoderm embryos, the relative position of
107 nuclei and the length of astral microtubules lead to the formation of short antiparallel Feo-decorated
108 microtubule overlaps. Furthermore, as a consequence of Feo crosslinking astral microtubules, a
109 mechanical connection is established that may control the distance between neighboring asters and
110 their associated nuclei.

111 During the last four syncytial nuclear cycles at the cortex, actin based pseudo-compartments that
112 drive membrane invagination – a physical barrier that is assembled and disassembled in every
113 division cycle (Kotadia et al., 2001; Mavrakis et al., 2009a) – is thought to guarantee nuclear
114 separation. Surprisingly, time-lapse confocal imaging of live embryos expressing either
115 Klp61F::GFP and Feo::mCherry (Fig. 1F, Suppl. Video 2) or Klp3A::GFP and Feo::mCherry (Fig.
116 1G, Suppl. Video 3), injected with Alexa647–Tubulin, revealed Feo colocalizing with Klp3A at
117 the spindle midzone (arrows) and spot-like signals between neighboring spindles (arrowheads) in
118 anaphase and telophase. On one hand, this observation confirms the combined activity of Feo and
119 Klp3A, whereby Feo binding to microtubule overlaps recruits Klp3A to the overlap (Bieling et al.,
120 2010; Subramanian et al., 2013). On the other hand, the signal foci indicate that antiparallel
121 microtubule overlaps occur between neighboring non-sister nuclei across actin furrows and
122 membrane invaginations. This observation led us to question the current paradigm that actin
123 pseudo-compartments prevent microtubule crosslinking between neighboring asters or nuclei. We

124 hypothesize from this localization data that the microtubule-based mechanical connection plays a
125 decisive role in nuclear positioning in preblastoderm and early blastoderm stage embryos.

126 ***Partial knockdown of Feo, Klp3A or Klp61F leads to defective nuclear delivery to the embryo***
127 ***cortex***

128 We wanted to understand the functional implication of the three microtubule binding proteins that
129 localize between non-sister nuclei, and if they are required for correct nuclear delivery to the cortex.
130 To this end, we perturbed the protein levels of Feo, Klp3A or Klp61F using an RNA interference
131 (RNAi) approach and UAS–Gal4 expression in the germline (Staller et al., 2013). We expressed
132 RNAi against these genes individually in the developing *Drosophila* oocyte (Suppl. Fig. 1A), while
133 expressing Jupiter::GFP, a microtubule reporter (Morin et al., 2001), and H2Av::RFP, a chromatin
134 reporter (Schuh et al., 2007). We exploited the expression kinetics of V32–Gal4 to drive the UASp–
135 RNAi constructs with peak in late oogenesis to prevent undesirable defects during stem cell
136 division. Fertilization in embryos depleted of Feo, Klp3A or Klp61F was similar to the control
137 embryos (data not shown). However, we were unable to determine the exact cycle number when
138 nuclei arrived at the cortex in knockdown embryos. Of note, the interval of division cycles
139 occurring at the cortex and in the embryo explants remained unaltered when compared to controls.
140 Under all knockdown conditions, we observed nuclei arriving later on average; ~45 min in
141 knockdown condition versus ~15 min in controls, following a 45 min egg laying period. In
142 knockdown embryos, nuclei were irregularly distributed at the cortex and sometimes missing
143 entirely at the posterior end, in contrast to the regular distribution seen in the control RNAi embryo
144 (Fig. 2A, Suppl. Fig. 1B). The nuclear density is reduced after knockdown as compared to the
145 control (Fig. 2B) but exhibited considerable variability between embryos, which we attributed to
146 the incomplete RNAi. Our analysis revealed embryos with larger areas lacking nuclei (Suppl. Fig.
147 2A), with anatomically eccentric (Suppl. Fig. 2B) and asymmetric nuclear distribution (Suppl. Fig.
148 2C). Overall, RNAi against Feo resulted in larger distribution changes than RNAi against Klp61F
149 despite similar average internuclear distance (Fig. 2B,C, Suppl. Fig. 2). The distribution of
150 internuclear distance was shifted towards longer distances for knockdown conditions, while RNAi
151 against Klp3A gave on average the strongest phenotype (Fig. 2C, Suppl. Fig. 2D). We also
152 observed a considerable reduction of fluorescence intensity of Klp3A::GFP at the midzone in Feo
153 knockdown embryos (Suppl. Fig. 1C). This confirms Klp3A being downstream of Feo binding to
154 microtubule overlaps (Bieling et al., 2010) and indicates that a reduction of Feo mRNA
155 concentration by half has a disproportionately stronger effect on Klp3A localization at microtubule
156 overlaps. The irregularity in nuclear position at the cortex increased as the cortical nuclear cycles

157 progressed (Suppl. Video 4). Occasionally in Feo knockdown embryos, we observed sister nuclei
158 fusing after mitosis and non-sister nuclear moving towards each other, leading to fusion of the
159 spindles and over-condensed chromatin. This likely occurs in preblastoderm cycles as well, leading
160 to fewer nuclei arriving at the cortex and contributing to nonuniformity. Conversely, fusion was
161 never seen in controls. In summary, the activity of all three microtubule associated proteins is
162 required in the preblastoderm embryo for correct delivery of nuclei to the embryo cortex. However,
163 Kinesin-5 is required for spindle assembly (Heck et al., 1993; Sawin et al., 1992) and, thus, the
164 phenotype can emerge due to assembly defects rather than post-mitotic nuclear separation. Because
165 depletion of Kinesin-5 led to a mild phenotype despite high knockdown efficiency (Suppl. Fig.
166 2A), and because of the functional relationship between Feo and Klp3A, we followed up on the
167 role of the latter two genes in maintaining internuclear distance

168 ***Developmental reset ex vivo reveals failure in nuclear distribution upon RNAi knockdown***

169 Our analysis of nuclear distribution during partial knockdown in the embryo suggests that Feo and
170 Klp3A are involved in nuclear delivery to the cortex. However, our knockdown approach *in vivo*
171 has two drawbacks that can lead to misinterpretation: (i) the three proteins play a role in spindle
172 midzone function, and their depletion may affect chromosome segregation in anaphase; (ii) The
173 RNAi expression occurs chronically during late oogenesis. Thus, the irregular distribution of nuclei
174 during cortical migration can be due to early sister chromatid separation errors, leading to missing
175 nuclei in the embryo center and exponentially fewer in subsequent division cycles. Alternatively,
176 inefficient nuclear separation following fertilization can lead to spindle fusion and mitotic errors.
177 To circumvent the inability to detect accumulated effects, we performed time-lapse imaging of
178 nuclear division cycles in embryo explants from preblastoderm embryos that were depleted of
179 either Feo or Klp3A. Because these explants contained only few dividing nuclei, we followed their
180 distribution, or the failure thereof, while mimicking the very beginning of preblastoderm embryo
181 development. We tracked individual nuclei undergoing division cycles and registered the
182 distribution and any fusion events between sister and non-sister nuclei (Fig. 3A). In explants from
183 control embryos, nuclei divide and distribute regularly in the entire explant (Fig. 3A, left, white
184 dashed circle) until a saturated nuclear distribution is reached and occasional mitotic failures in the
185 subsequent cycle are observed. The nuclear density at saturation is comparable to nuclear cycle 10
186 in the intact embryo (1800–2000 nuclei/mm^2)(Foe and Alberts, 1983), corresponding to an
187 internuclear distance of ~25 µm (hexagonal approximation). Strikingly, the nuclei from Feo and
188 Klp3A knockdown embryos also divide consecutively. The average distance between sister nuclei
189 and between non-sister nuclei was lower in the test RNAi as compared to the control (Fig. 3B,C).

190 However, the nuclear position after mitotic separation was maintained in the Feo RNAi while
191 knockdown of Klp3A led to frequent spindle fusion at a comparable nuclear density and
192 accumulation of mitotic failure. Interestingly, spindle length decreased upon depletion of Feo (Fig.
193 3A), but we did not observe significant decrease in spindle length upon Klp3A depletion as reported
194 earlier, most likely due to inefficient knockdown as compared to deletion (Williams et al., 1995).
195 In summary, the reduction of Feo expression leads to reduced nuclear separation between sister
196 nuclei and incomplete occupation of nuclei within the explant. However, while a reduction of Feo
197 sustains mitotic divisions, Klp3A knockdown produces a spindle fusion phenotype. It is possible
198 that the absence of Klp3A causes microtubule overlap over-growth and, despite crosslinking by
199 Feo and other MAPs, these long overlaps are not mechanically stiff.

200 ***Displacement of nuclei is rescued in control but not in Feo RNAi embryo explants***

201 To test the model of an astral microtubule crosslinker-based separation mechanism for non-sister
202 nuclei, we took advantage of the amenability of embryo explants for mechanical manipulation and
203 designed an acute perturbation approach. We asked how Feo relocalizes when the distance between
204 two interphase nuclei is manually reduced. Finally, we asked whether, under a Feo knockdown
205 condition, nuclei could adjust their position when brought in close proximity prior to division. To
206 address these questions, we performed contact micromanipulation and changed the positions of
207 two non-sister nuclei that were exiting mitosis (Fig. 4A), during the non-mitotic phase which is
208 amenable to manipulation (Telley et al., 2012). Following manipulation (Fig. 4B, arrowheads),
209 nuclei were typically in interphase, when Feo is not expected to localize due to cycle regulation.
210 Nonetheless, we registered strong localization of Feo::mCherry in anaphase and telophase of the
211 next cycle exclusively in the region between the manipulated nuclei (Fig. 4B, arrow) while asters
212 from distant, non-manipulated nuclei did not recruit the microtubule crosslinker detectably. Next,
213 we quantified nuclear separation of two neighboring nuclei dividing into four daughter nuclei by
214 determining the four final positions (Fig. 4C), arranging these positions as a quadrilateral, aligning,
215 annotating and overlaying them in a common coordinate system (Fig. 4D,E) and calculating area
216 (Fig. 4F) and lateral distances (Fig. 4G,H). We performed these measurements under the control
217 RNAi condition for nuclei in a large unoccupied cytoplasmic space, in a saturated space where
218 several nuclei have spread through the entire explant, and in a crowded explant representing one
219 more division cycle after saturation; this differentiated comparison takes into account nuclear
220 density dynamics in cycling explants, as described in the previous section (Fig. 3). We found that
221 the area of nuclear separation after manipulation is lower than in the non-manipulated and saturated
222 space but indifferent from the crowded control (Fig. 4F). The manipulated nuclei divided and

223 separated their daughter nuclei at ~15 µm while the distance between non-siblings was maintained
224 at ~25 µm (Fig. 4G,H) (Telley et al., 2012), phenocopying the minimal separation seen in crowded
225 explants for which distance maintenance is challenging. Interestingly, these separation distances
226 are similar to what was reported for the blastoderm embryo (Kanesaki et al., 2011). Finally, we
227 performed the manipulation of nuclear position in Feo-depleted explants expressing Jupiter::GFP
228 and H2Av::RFP. In these experiments, after manipulation, the daughter nuclei moved towards each
229 other rather than apart (Suppl. Fig. 3C). The separation of siblings was approximately the nuclear
230 diameter (~7 µm) (Fig. 4G, dashed line) and the separation of non-siblings was ~10 µm (Fig. 4H).
231 We conclude that acute repositioning of nuclei is detected by the separation machinery, as reported
232 by Feo, and is counteracted to prevent spindle fusion or aggregation of nuclei. In other words, Feo
233 is required to prevent nuclear collisions.

234 ***Nuclear separation in the syncytium requires astral microtubule crosslinking by Feo***

235 Feo is a dimer and, *in vitro*, has high affinity for binding two antiparallel microtubules (Bieling et
236 al., 2010; Subramanian et al., 2013; 2010). In this function, Feo can generate a repulsive
237 mechanical link – an apparent stiffness – which prevents concentric movement and eventual
238 contact of neighboring nuclei. This model predicts a lower repulsion stiffness in the presence of a
239 monomeric construct of Feo, which binds to the same microtubule lattice binding site as the full-
240 length dimer but does not crosslink the antiparallel microtubules. We expect that this molecular
241 competition leads to weaker crosslinking and can be measured as shorter internuclear distance,
242 irregular separation or frequent nuclear contacts. Thus, we designed two protein expression
243 constructs; one containing the full *feo* coding sequence (sFeoFL::GFP-His_6), the other lacking the
244 N-terminal, putative dimerization domain (sFeoN::GFP-His_6), and fused them to a C-terminal GFP
245 and a His_6 tag sequence (Fig. 5A,C). Proteins were expressed in *E.coli*, affinity-purified and
246 dialyzed into embryo explant compatible buffer (Telley et al., 2013) (Suppl. Fig. 4A). Full-length
247 Feo::GFP forms dimers, as was reported for vertebrate homologs (Bieling et al., 2010;
248 Subramanian et al., 2013; 2010), while the truncated protein is dimerization deficient and forms
249 monomers or weak dimers (Suppl. Fig. 4B). When the full-length protein was injected at nanomolar
250 concentration into embryos, GFP signal localized at the central spindle (Fig. 5B, arrow). As in
251 transgenic embryos (Fig. 1F,G, arrowheads), we also detected small foci of green fluorescence
252 between neighboring nuclei (Fig. 5B, arrowheads), suggesting that the purified protein and the
253 transgenic construct localize identically and under cell cycle control with fluorescence
254 disappearing in interphase and reappearing during telophase of the following cycle (Suppl. Video
255 5 and 6). Though faint, the truncated protein construct localized at the spindle midzone, not in the

256 cycle following injection but the subsequent division cycle (Fig. 5D, Suppl. Fig. 4C, Suppl. Video
257 7). Injection of full-length Feo::GFP maintained regular nuclear delivery to the embryo cortex
258 while injection of truncated Feo::GFP caused unnatural spindle contacts and nuclear separation
259 defects (Suppl. Fig. 4C middle, Suppl. Video 7). Furthermore, when the full-length protein was
260 injected into Feo RNAi embryos the defective nuclear distribution was rescued to a large extent
261 (Suppl. Fig. 4D). Nuclei arrived at the embryo cortex more symmetrically between anterior and
262 posterior ends (Fig. 5E), in a less skewed distribution (Fig. 5F) and with more uniform internuclear
263 distance (Fig. 5G) as compared to mock-injected Feo RNAi embryos. Owing to the variability of
264 injection and knockdown efficiency, we fully recovered nuclear density to a normal level in two
265 embryos and significantly increased nuclear density in the remaining five embryos (Fig. 5H).
266 Notably, the injected protein pool is stable for at least 90 minutes, throughout several division
267 cycles. In summary, we show that a GFP-tagged full-length protein construct localizes correctly
268 and rescues the gene knockdown in the germline. We conclude that it is functionally identical to
269 the endogenous protein that is maternally deposited in the egg and stable during syncytial
270 development.

271 Finally, having designed and purified the truncated and the full-length protein with identical
272 procedures, we asked how nuclear separation changes upon excess of the dimerization deficient
273 Feo protein, added at 100–200 nM final concentration to wildtype embryo explants containing one
274 or two nuclei. As control condition, we injected the full-length protein at the same final
275 concentration into embryo explants, and despite this perturbation the explant supported normal
276 nuclear separation and distribution (Fig. 5I, left). Conversely, adding the truncated protein construct
277 worsened nuclear separation considerably after chromosomes segregated. Here, in contrast to the
278 control condition, nuclei did not occupy the entire explant space after consecutive divisions. The
279 short internuclear distance led to unnatural chromosome aggregation, fusion and eventually to
280 mitotic failure. Nuclear separation of two neighboring non-sister nuclei, as measured by the
281 quadrilateral area defined by their position, was significantly smaller than in control divisions in
282 the presence of full-length Feo protein (Fig. 5J,K). We conclude that microtubule crosslinking by
283 Feo, in the presence of Klp3A, generates a repulsive mechanical link between microtubule asters.
284 Thus, it lies at the heart of nuclear separation maintenance during the multinucleated 1-cell stage
285 of *Drosophila* embryo development.

286 Discussion

287 A cornerstone of embryonic development is the formation of a polarized epithelium. Plants and
288 many invertebrates achieve this developmental stage with a unicellular embryo undergoing nuclear

289 proliferation followed by cellularization, a specialized form of cytokinesis (Hehenberger et al.,
290 2012; Lecuit and Wieschaus, 2000). Recently, the molecular building blocks and morphogenetic
291 characteristics of cellularization have also been identified as part of the life cycle of a non-animal
292 eukaryote (Dudin et al., 2019). The offspring of *Sphaeroforma arctica* arises from nuclear
293 proliferation, compartmentalization, and plasma membrane invagination generating a proto-
294 epithelium from which newborn cells detach. These observations support the hypothesis that
295 epithelia evolutionary predate animals (Dickinson et al., 2012). We propose that correct
296 compartmentalization and generation of uninuclear offspring necessitates robust nuclear
297 separation. If warranted true, then a separation mechanism must have coevolved with the origin of
298 epithelia and was essential for the emergence of multicellularity.

299 Nuclear proliferation in a coenocyte poses a new challenge: How does the cell safeguard the
300 separation and prevent contact of nuclei while their number increases? Two solutions seem
301 plausible. On one hand, the cell may control the division axes and separate daughter nuclei along
302 linear paths which do not cross. On the other hand, the cell may constrain internuclear distance
303 independent of separation trajectories. Consider two nuclei that are about to divide and separate
304 their progeny along the spindle axis (Fig. 6A). In a 3-dimensional space, none of the daughter
305 nuclei may collide unless the spindle axes are both coplanar and non-parallel. Typically, nuclei
306 migrate only 10–15µm away from the original spindle center before dividing again (Telley et al.,
307 2012). This geometric constraint reduces configurations that produce colliding trajectories in a 2-
308 dimensional topology to about 40% of all possible spindle axis orientations, so that axes intersect
309 at an angle between zero (collinear) and 70º (Fig. 6B). Adding complexity, spindles in a network
310 with optimal packing face a number of neighbors (6 in 2D, 12 in 3D) (Fig. 6C). Thus, a
311 synchronously dividing spindle network will inevitably produce colliding trajectories of daughter
312 nuclei. It is therefore necessary that, instead of controlling division axes, the cell controls nuclear
313 proximity independent of the relative orientations they divide (Fig. 6B). This enables the syncytial
314 embryo to divide hundreds of nuclei synchronously and distribute them to any unoccupied position.
315 Here, we demonstrate a molecular mechanism that responds to short internuclear distances in the
316 syncytium with a microtubule dependent repulsion. Each nucleus is associated with a radial array
317 of microtubules nucleated by the centrosome, which duplicates and forms the two spindle poles in
318 the next division. Prior, however, this microtubule aster guides nuclear migration and grows large
319 enough to encounter microtubules from neighboring asters that migrate as well. This encounter
320 leads to interdigitation of the microtubule plus–ends (antiparallel overlaps) and forms binding sites
321 for crosslinking proteins. Our data shows that Feo, the PRC1 homolog in *Drosophila* and

322 antiparallel microtubule crosslinker, plays a central role in defining a minimal internuclear distance
323 in the syncytial *Drosophila* preblastoderm embryo.

324 Vertebrate PRC1 is a microtubule binding protein with high turnover kinetics and at least 28 times
325 higher affinity for antiparallel microtubule overlaps than for single microtubules (Bieling et al.,
326 2010). This biochemical property, together with fluorescent labeling, renders PRC1 homologs
327 reliable reporters for microtubule aster overlaps in live cell imaging assays (Nguyen et al., 2014).
328 PRC1 crosslinking antiparallel microtubules generates a high affinity binding site for the motor
329 protein Kinesin-4 (Kif4/Xklp1/Klp3A) at the overlap (Bieling et al., 2010; Kurasawa et al., 2004).
330 *In vitro*, in addition to maintaining a stable overlap length, co-activity of PRC1 and Xklp1 cause
331 buckling of overlapping microtubules which are immobilized at their minus end (Bieling et al.,
332 2010). In a sliding assay of taxol-stabilized microtubules, in which microtubules in solution and
333 glass-immobilized microtubules form pairs cross-linked by PRC1, the antiparallel pairs of
334 microtubules are slid apart by Kif4 (Wijeratne and Subramanian, 2018). This is reminiscent of
335 plus–end directed sliding of Kinesin-5 (Kapitein et al., 2005) and explains the requirement of PRC1
336 orthologs for spindle elongation in several species (Khmelinskii et al., 2009; Schuyler et al., 2003;
337 Wang et al., 2015; Zhu et al., 2006). Indeed, plus–end overlapping microtubules have an apparent
338 mechanical stiffness that is governed by molecular friction and motor activity (Forth et al., 2014;
339 Wijeratne and Subramanian, 2018). An assembly of tens of such microtubule pairs generates
340 sufficient mechanical resistance against compressive forces in the nanonewton range, enough to
341 keep two spherical organelles of 5–8 µm diameter and attached to the microtubule minus–ends
342 (MTOC) well separated (Lele et al., 2018). Thus, modular upscaling of a single pair into
343 overlapping radial arrays illustrates how the sliding mechanism of a Feo and Klp3A decorated
344 antiparallel microtubule pair produces a repulsion between two syncytial nuclei.

345 Feo::GFP expressed in the transgenic line, or supplemented as purified protein, exhibited focal
346 fluorescence signals in the blastoderm embryo and in the explant from preblastoderm embryos.
347 Here we showed that the length of these signal foci is surprisingly short and uniform. According
348 to *in vitro* data, and neglecting any regulation other than affinity and stabilization activity for the
349 underlying microtubule overlap to maintain such a short length, the concentration of Kinesin-4 in
350 the cytoplasm must be at least one magnitude in excess of Feo (Bieling et al., 2010). Moreover,
351 partial depletion of Feo by RNAi abolished the signal of Klp3A::GFP below detection, thus
352 considerably reducing the bound fraction of Klp3A at the central spindle. In the embryo, while
353 confirming their already established localization at the spindle midzone (D'Avino et al., 2007;
354 Kwon et al., 2004; Page and Hawley, 2005; Wang et al., 2015; Williams et al., 1995), we recorded

355 Klp3A::GFP signal colocalizing with Feo::mCherry in areas between neighboring spindle asters.
356 However, we could not clearly assess the localization of Klp3A in explants from preblastoderm
357 embryos due to the low signal intensity. A single-copy tagged Klp3A construct expressed with the
358 endogenous promoter failed to provide sufficient signal, and we decided to work with
359 overexpression constructs (Sarov et al., 2016). This indicates that the microtubule overlap–bound
360 fraction of endogenous Klp3A is comparatively small despite the molar excess in the cytosol as
361 derived from overlap length. Together, these observations point at a protein interaction network
362 localized at antiparallel microtubule overlaps that is sensitive to small changes of Feo. As Feo binds
363 microtubule overlaps independently (Bieling et al., 2010), the phenotypes in intact embryos and in
364 explants can arise due to disproportionate Klp3A perturbation downstream of Feo. In summary,
365 our live-cell microscopy data from blastoderm embryos and preblastoderm embryo explants
366 support a 'central spindle model' built from individual pairs of microtubules crosslinked and
367 length-regulated by Feo and Klp3A (Bieling et al., 2010). More importantly, we show how
368 overlapping microtubules in the aster–aster interaction zone (Nguyen et al., 2014) form midzone–
369 analogous cytoskeletal assemblies that persist throughout blastoderm development. This is
370 particularly intriguing given that, at the embryo cortex from cycle 10 onwards, actin-based pseudo-
371 furrows are thought to form pre-cellular compartments that prevent nuclear contact (Karr and
372 Alberts, 1986; D. R. Kellogg et al., 1988; Lecuit, 2004; Mavrakis et al., 2009b). In the early
373 blastoderm cycles, however, this compartmentalization may not yet be efficient enough to
374 safeguard nuclear separation, and astral microtubule crosslinking persists as dominant mechanism.
375 This interpretation is further supported by an earlier observation in mutants of the maternal-effect
376 gene *sponge*, embryos of which do not form actin caps and pseudo-furrows in blastoderm stage but
377 depict a homogenous nuclear distribution in cycle 10–11 (Postner et al., 1992).

378 Feo is essential for central spindle assembly and cytokinesis in somatic cells, containing two Cdk
379 phosphorylation sites (Vernì et al., 2004). Feo, like PRC1 in human cells and Ase1p in fission
380 yeast, is under cell cycle control and undergoes phosphorylation dependent localization from low
381 intensity decoration of metaphase spindle microtubules to a strong localization at the central
382 spindle in anaphase and telophase (Khmelinskii et al., 2009; Polak et al., 2017; Subramanian et al.,
383 2013; Wang et al., 2015; Zhu et al., 2006). In the present work, we showed that the focal
384 localization of Feo and Klp3A between neighboring nuclei is in synchrony with central spindle
385 localization. It is in this phase of the division cycle when expanding spindles and separating nuclei
386 cause a large spatial perturbation to the positional distribution (Kanesaki et al., 2011; Lv et al.,
387 2020). Thus, a dual role for Feo under cell cycle control emerges; while it targets the central spindle

388 at anaphase onset – forming the spindle midbody – it also binds to astral microtubule overlaps in a
389 phase during which collision prevention is most needed.

390 In *Drosophila* embryos, spindle elongation at anaphase B is powered by the sliding activity of
391 Klp61F (Brust-Mascher et al., 2009). Following the mechanism proposed by Baker et al. (1993),
392 and because Klp61F is a candidate crosslinker and slider of overlapping astral microtubules, we
393 performed RNAi knockdown in the germline. Reduction of Klp61F levels to 19% of native levels
394 led to lower density and non-uniform delivery of nuclei to the embryo cortex, confirming its
395 essential role during preblastoderm development. However, owing to the established role of
396 Klp61F in anaphase, the RNAi phenotype can emerge as a consequence of multiple chromosome
397 segregation failures that were undetectable in the preblastoderm embryo. Here, the embryo explant
398 assay overcomes an experimental limitation and enables time-lapse image acquisition of uni- or
399 binuclear explants undergoing multiple divisions. Consequently, we could confirm that Klp61F
400 knockdown led to more frequent division failures rather than shorter nuclear separation. Still,
401 Klp61F and Feo can functionally cooperate in crosslinking astral microtubules because both
402 proteins recognize and bind to microtubule pairs, though with different preference for microtubule
403 orientation (Bieling et al., 2010; Kapitein et al., 2005; E. H. Kellogg et al., 2016; Subramanian et
404 al., 2010). Interestingly, a recent study demonstrated that, while Feo modulates binding and
405 localization of Klp61F at the spindle midzone in anaphase, Klp61F cannot functionally rescue the
406 absence of Feo (Wang et al., 2015). Presumably, Ase1p/PRC1/Feo binding to microtubule overlaps
407 creates a protein binding hub for motors and regulators (Bieling et al., 2010; D'Avino et al., 2007;
408 Hu et al., 2012; Khmelinskii et al., 2009; Sasabe and Machida, 2006; Subramanian et al., 2013).
409 This property has not been demonstrated for Kinesin-5 orthologs. Together, the collection of our
410 and other evidence concludes that Klp61F is not at the core of astral microtubule driven nuclear
411 separation.

412 Lastly, the reader may wonder how astral microtubule overlap crosslinking by Feo and Klp3A
413 defines the internuclear distance metric, leading to a distribution of syncytial nuclei with high
414 regularity. In an earlier study, Telley et al. (2012) showed that microtubule aster size varies
415 throughout the nuclear division cycle, reaching a maximum of 11 ± 3 μm in telophase. Herein, the
416 aster size represents the length distribution of microtubules which, for dynamic microtubules with
417 non-growing minus–end, is well approximated with an exponential distribution (Howard, 2001).
418 We assume that two microtubules from neighboring asters grow at least to average length, overlap
419 with their plus–ends and are collinear. If the stabilized overlap length is ~1 μm, then the total length
420 from centrosome to centrosome is on average 21 ± 4 μm. Considering that a centrosome is ~1 μm

421 large, and that a nucleus in late telophase is 5 ± 1 μm in diameter, the total distance between the
422 centers of neighboring nuclei is 28 ± 4 μm. This estimate is in good agreement with the internuclear
423 distance distribution measured from center to center of each nucleus (Fig. 3c), the minimal non-
424 sibling internuclear distance in extract (Fig. 4h) and earlier reported separation distances of
425 daughter nuclei (Telley et al., 2012). Thus, the short antiparallel overlap length of microtubules
426 from neighboring asters and the microtubule length distribution are sufficient to explain the
427 geometry of nuclear distribution in the *Drosophila* syncytial embryo.

428 **Star★Methods**

429 **Resource Availability**

430 **Lead contact**

431 Further information and requests for reagents should be directed to and will be fulfilled by the lead
432 contact, Dr. Ivo A. Telley (itelley@igc.gulbenkian.pt).

433 **Material and dataset availability**

434 All unique reagents, raw data and MATLAB® codes generated in this study are available upon
435 request without restriction.

436 **Experimental Model and Subject Details**

437 **D. melanogaster**

438 Rearing of flies for general maintenance was done as previously described (Stocker and Gallant,
439 2008). The following fly lines were used to make recombinants or trans-heterozygotes:
440 Jupiter::GFP (BDSC# 6836), Jupiter::mCherry (generated by and obtained from Nick Lowe in
441 D. St Johnston's lab, The Gurdon Institute), pUbq>Spd2::GFP (gift from M. Bettencourt-Dias,
442 IGC), H2Av::RFP (BDSC# 23650), Feo::GFP (BDSC# 59274), Feo::mCherry (BDSC# 59277),
443 Klp61F::GFP (BDSC# 35509), Klp3A::GFP (VDSC# 318352), RNAi targeting Feo (BDSC#
444 35467), RNAi targeting Klp3A (BDSC# 40944), RNAi targeting Klp3A (BDSC# 43230), RNAi
445 targeting Klp61F (BDSC# 35804), RNAi targeting Klp61F (BDSC# 33685), RNAi targeting
446 mCherry (BDSC# 35785), UASp–GFP (BDSC# 35786).

447 **Method details**

448 **RNAi experiments**

449 Knockdown experiments were performed using the TRiPGermline fly lines for RNAi in germline
450 cells (Perkins et al., 2015). The UAS-hairpin against a gene of interest was expressed using V32–
451 Gal4 (gift from M. Bettencourt Dias) at 25ºC. The expression profile of V32–Gal4 in the oocyte

452 was assessed by dissecting ovaries of flies expressing UASp–GFP at 25ºC and comparing GFP
453 expression at different developmental stages with fluorescence microscopy.

454 **Sample preparation and extraction**

455 Embryos were collected from apple juice agar plates mounted on a fly cage. They were
456 dechorionated in 7% sodium hypochlorite solution, aligned and immobilized on a clean coverslip
457 using adhesive dissolved in heptane and covered with halocarbon oil (Voltalef 10S). Extraction of
458 cytoplasm from individual embryos and generation of explants was performed on a custom-made
459 microscope as previously described (de-Carvalho et al., 2018; Telley et al., 2013).

460 **Quantitative PCR**

461 To measure the transcript levels of *feo*, *klp3A* and *klp61F*, total RNA was extracted following
462 standard procedures (PureLink RNA Mini Kit, Ambion) from embryos collected after 40 minutes
463 of egg laying. A cDNA library was made from Oligo(dT)12–18 as described in the manufacturer's
464 protocol (Transcriptor First Strand cDNA Synthesis Kit, Roche). Quantitative PCR was performed
465 using Quantifast SYBR Green PCR Kit (204052) and QuantiTect Primers for *feo* (QT00919758)
466 in Feo RNAi, *klp3A* (QT00497154) in Klp3A RNAi (40944 and 43230) and *klp61F* (QT00955822)
467 in Klp61F RNAi(35804 and 33685). Actin (QT00498883) was used as a housekeeping gene
468 control.

469 **Purification of sFeoFL::GFP and sFeoN::GFP**

470 The full coding sequence of the *feo* gene fused to a C-terminal GFP tag, was synthesized and codon
471 optimized by NZYTech, referred to herein as sFeoFL::GFP. The DNA was cloned into the vector
472 pET-21a containing a C-terminal His_6-tag, and transformed into *E.coli Rosetta* cells. The coding
473 sequence of the *feo* gene without the initial 73 N-terminal residues, referred here as truncated
474 sFeoN::GFP construct, was amplified from the synthesized sFeoFL::GFP construct and re-cloned
475 into the pET-21a vector. Both proteins were produced by IPTG induction at 25ºC. After 4h of
476 incubation, the cells were harvested and resuspended in lysis buffer (100mM K-HEPES pH 7.4,
477 500 mM NaCl, 10% glycerol, 0.1% Triton X-100, 3 M urea, supplemented with protease inhibitors
478 (Roche) and 100U of DNAse type I (NZYTech)). The cells were lysed using the digital sonifier®
479 (SLPe, Branson) at 70% amplitude with 6 pulses of [30 sec on]–[30 sec off] and clarified by
480 centrifugation at 30,000g for 45 minutes at 4ºC. For purification of the truncated construct, the
481 supernatant was loaded onto a 5 ml HiTrap Chelating HP (GE Healthcare) charged with 0.1 mM
482 $NiCl_2$ and equilibrated with wash buffer (100 mM K-HEPES pH7.4, 500 mM NaCl, 10% glycerol,
483 40 mM imidazole, 1 mM 2-mercaptoethanol), extensively washed with this buffer and eluted with

484 elution buffer (100 mM K-HEPES pH7.4, 500 mM NaCl, 10% glycerol, 500 mM imidazole, 1 mM
485 2-mercaptoethanol) throughout a gradient of 6 CV. For purification of the full-length construct, the
486 supernatant was loaded onto a 1 ml HiTrap TALON crude (GE Healthcare) charged with 50 mM
487 $CoCl_2$ and equilibrated with wash buffer (100 mM K-HEPES pH 7.2, 500 mM NaCl, 10% glycerol,
488 5 mM imidazole, 1 mM 2-mercaptoethanol), extensively washed with this buffer and eluted with
489 elution buffer (100 mM K-HEPES pH 7.2, 500 mM NaCl, 10% glycerol, 150 mM imidazole, 1
490 mM 2-mercaptoethanol), throughout a gradient of 20 CV. Fractions containing the protein of
491 interest were pooled, the buffer exchanged into embryo explant compatible buffer (100 mM K-
492 HEPES pH 7.8, 1 mM $MgCl_2$, 100 mM KCl) using a PD-10 desalting column (GE Healthcare) and
493 concentrated using a 50K MWCO Amicon® Ultracentrifugal filter (Merck). The purifications were
494 performed using the ÄKTApurifier protein purification system (GE Healthcare) and the
495 chromatographic profile of both proteins was followed by measuring the absorbance at 280 nm,
496 254 nm and 488 nm in the UV-900 monitor. The size exclusion method resulted in Feo constructs
497 strongly associated to an unknown contaminant at ~50 kDa. The concentration of each construct
498 was estimated ~50% of the total measured protein concentration based on band analysis of SDS-
499 PAGE. Total protein concentrations were measured with a NanoDrop2000 UV-Vis
500 spectrophotometer (ThermoFisher).

501 **SDS PAGE, Native PAGE and Blotting with quantification**

502 Polyacrylamide gels for electrophoresis and Coomassie-staining were made with 15% SDS.
503 Molecular mass was estimated by linear regression of $\log_{10}(M_W$ [Da]) as a function of the migration
504 distances [cm] of the ladder (BioRad, 161-0375). To determine the dimerization of sFeoFL::GFP
505 and sFeoN:GFP a Western Blot was generated from a 4-12% gradient SDS and a Native
506 polyacrylamide gel side-by-side using a mouse anti-GFP antibody (Roche Nr. 11814460001) at
507 1:500 dilution. The molecular mass of the protein samples was estimated using a linear regression
508 of $\log_{10}(M_W$ [Da]) as a function of the migration distances [cm] of the ladder (NZYTech MB090);
509 in the SDS gel a regression was performed on the entire ladder while for the Native gel only the
510 higher molecular mass ladder (100–245 kDa) was considered.

511 **Addition of exogenous purified proteins**

512 Purified porcine Tubulin (Cytoskeleton) was labeled with Alexa-647 (Invitrogen, ThermoFisher)
513 following a published protocol (Hyman, 1991) and injected into embryos or explants at 0.3–0.8
514 mg/ml. Purified sFeoFL::GFP and sFeoN::GFP were injected at 2 mg/ml in EC buffer in embryos
515 or explants. This concentration was a result from a series of titrations over a magnitude of different
516 concentrations and assessing phenotype or rescue. For embryos, the injected volume assumed a

517 spherical shape with diameter D ≈ 0.018 mm, resulting an injection volume of 3.05 x 10^{-6} mm^3.
518 The average length and width of the embryo are 0.5 mm and 0.2 mm, respectively (Markow et al.,
519 2008). Assuming an ellipsoid geometry for the embryo, its volume is ~10^{-2} mm^3. Thus, the final
520 concentration of injected protein after equilibration in the entire embryo was 5–6 nM. For explants,
521 both protein constructs were added to explant cytoplasm at 1:200 (vol/vol), resulting in a final
522 concentration in the cytoplasm of 100–200 nM. Importantly, such an excess of full-length Feo
523 protein preserved nuclear divisions and distribution.

524 Quantification and Statistical Analysis

525 Image acquisition, processing and analysis

526 Transmission light microscopy images were obtained with a 10x 0.25NA objective, and the
527 polarizer and analyzer of the microscope in crossed configuration. Time-lapse confocal
528 fluorescence Z stacks were acquired on a Yokogawa CSU-W1 spinning disk confocal scanner with
529 488 nm, 561 nm and 640 nm laser lines. Images of whole embryos were acquired with a 40x 1.3NA
530 oil immersion objective. Images of embryo explants were acquired with a 60x 1.2NA or a 40x
531 1.15NA water immersion objective. Images were recorded with an Andor iXon3 888 EMCCD
532 1024x1024 camera with 13 µm square pixel size, and a 2x magnification in front of the camera.
533 Image processing i.e. making Z-projections, image cropping, image down-sampling, and video
534 generation, was performed in Fiji (Schindelin et al., 2012). Whole embryo images for knockdown
535 experiments were obtained by pairwise stitching using a plugin in Fiji.

536 The fluorescence signal of Feo::GFP in explants was analyzed with the line profile tool in Fiji.
537 First, images of dividing nuclei during anaphase or telophase were filtered with a Gaussian kernel
538 ($\sigma = 1.2$). Spot-like signals located between non-sibling nuclei were identified and, where spots
539 were non-circular, a line was drawn along the longer axis. The angle of the line relative to the
540 image coordinate system was recorded, and an intensity profile was generated. Profiles were
541 aligned relative to the position of highest intensity and averaged. For each image, an intensity
542 profile from a location void of microtubule signal was generated to obtain the background and the
543 standard deviation of Feo::GFP intensity. Finally, the size of the spot was determined by calculating
544 the width of the curve where the intensity was higher than two times the standard deviation of the
545 background. The angle of every profile line was transformed relative to the closer of the two axes
546 that connect the centrosome of one nucleus with the centrosome of the two neighboring sister nuclei
547 (Fig. 1C) termed as angle θ. A probability density plot from all measured angles was generated in
548 MATLAB®.

549 The nuclear density in whole embryo images was obtained by measuring the area of the visible
550 part of the embryo after manually tracing the border and dividing the number of nuclei by this area.
551 The localization of nuclei in whole embryos was performed manually in Fiji. The precision of
552 localization was 0.25 µm (intra-operator variability). Localization coordinates were imported into
553 MATLAB® and transformed with respect to the coordinate system of the embryo, as defined by
554 the anterior pole as coordinate origin, and the anterior-posterior axis as *x*-axis. The first-order
555 internuclear distances were obtained from the triangulation connectivity list ('delaunay' function),
556 while excluding any edge connections, and by calculating the distance between the remaining
557 connections. The cumulative distribution function of internuclear distances from individual
558 embryos was obtained with the 'ecdf' function in MATLAB®. An average cumulative distribution
559 function from several embryos was generated after pooling all distances together. Next, the
560 deviation of the centroid of nuclear positions from the anatomical center of the embryo was
561 obtained using the formula:

562 $$[M_x, M_y] = [C_x, 0] - \left[\frac{1}{n}\sum_{i=1}^{n} x_i\,, \frac{1}{n}\sum_{i=1}^{n} y_i\right]$$

563 whereby an estimate for the anatomical center of the embryo, $[C_x, 0]$ with respect to the embryo
564 coordinate system, is given by half the pole-to-pole distance on the *x*-axis and zero on the *y*-axis.
565 The third-order moment of the distribution of nuclear coordinates was calculated with the
566 'skewness' function in MATLAB®, providing a measure for left-right asymmetry.

567 The measurement of inter-nuclear distances in embryo explants was performed manually in Fiji.
568 The precision of distance measurement was ±0.12 µm as determined by repeated measurement
569 (intra-operator variability). The intensity profile plots of Klp3A::GFP in the Feo RNAi background
570 were obtained using the line profile tool in Fiji, by drawing a line between daughter nuclei in the
571 red (H2Av::RFP) channel and generating an intensity profile plot in the green channel, aligning
572 these profiles according to the peak intensity and averaging profiles from different locations and
573 embryos.

574 Plots of aligned quadrilaterals were generated with MATLAB® by coordinate transformation. The
575 area was calculated using Gauss' trapezoidal formula for general polygons:

576 $$A = \frac{1}{2}\left|\sum_{i=1}^{n-1} x_i y_{i+1} + x_n y_1 - \sum_{i=1}^{n-1} x_{i+1} y_i + x_1 y_n\right|$$

while $n = 4$ for 'quadrilaterals'. For each quadrilateral, representing two sets of dividing nuclei, the average of the two involved mitotic separation distances and the average of the two involved non-sibling separations were calculated and plotted. All graphs were made with MATLAB®.

Statistical analysis

We have plotted, unless otherwise mentioned, the distribution of raw data or cumulative probabilities. Sample sizes and the number of experimental repeats are reported in the figure legends. A Wilcoxon rank-sum test was performed with MATLAB® starting with a significance level $\alpha = 0.05$.

References

Almonacid, M., Ahmed, W.W., Bussonnier, M., Mailly, P., Betz, T., Voituriez, R., Gov, N.S., Verlhac, M.-H., 2015. Active diffusion positions the nucleus in mouse oocytes. Nature Cell Biology 17, 470–479. doi:10.1038/ncb3131

Almonacid, M., Jord, Al, A., El-Hayek, S., Othmani, A., Coulpier, F., Lemoine, S., Miyamoto, K., Grosse, R., Klein, C., Piolot, T., Mailly, P., Voituriez, R., Genovesio, A., Verlhac, M.-H., 2019. Active Fluctuations of the Nuclear Envelope Shape the Transcriptional Dynamics in Oocytes. Dev. Cell 51, 145–157.e10. doi:10.1016/j.devcel.2019.09.010

Baker, J., Theurkauf, W.E., Theurkauf, W.E., Schubiger, G., 1993. Dynamic changes in microtubule configuration correlate with nuclear migration in the preblastoderm Drosophila embryo. J. Cell Biol. 122, 113–121.

Bieling, P., Telley, I.A., Surrey, T., 2010. A minimal midzone protein module controls formation and length of antiparallel microtubule overlaps. Cell 142, 420–432. doi:10.1016/j.cell.2010.06.033

Bone, C.R., Starr, D.A., 2016. Nuclear migration events throughout development. Journal of Cell Science 129, 1951–1961. doi:10.1242/jcs.179788

Bringmann, H., Skiniotis, G., Spilker, A., Kandels-Lewis, S., Vernos, I., Surrey, T., 2004. A kinesin-like motor inhibits microtubule dynamic instability. Science 303, 1519–1522. doi:10.1126/science.1094838

Brust-Mascher, I., Sommi, P., Cheerambathur, D.K., Scholey, J.M., 2009. Kinesin-5-dependent poleward flux and spindle length control in Drosophila embryo mitosis. Mol. Biol. Cell 20, 1749–1762. doi:10.1091/mbc.e08-10-1033

Callaini, G., Dallai, R., Riparbelli, M.G., 1992. Cytochalasin induces spindle fusion in the syncytial blastoderm of the early Drosophila embryo. Biol. Cell 74, 249–254.

Cheerambathur, D.K., Brust-Mascher, I., Civelekoglu-Scholey, G., Scholey, J.M., 2008. Dynamic partitioning of mitotic kinesin-5 cross-linkers between microtubule-bound and freely diffusing states. J. Cell Biol. 182, 429–436. doi:10.1083/jcb.200804100

Cheerambathur, D.K., Gassmann, R., Cook, B., Oegema, K., Desai, A., 2013. Crosstalk between microtubule attachment complexes ensures accurate chromosome segregation. Science 342, 1239–1242. doi:10.1126/science.1246232

Dassow, von, G., Schubiger, G., 1994. How an actin network might cause fountain streaming and nuclear migration in the syncytial Drosophila embryo. J. Cell Biol. 127, 1637–1653.

617 Dassow, von, G., Verbrugghe, K.J.C., Verbrugghe, K.J., Miller, A.L., Sider, J.R., Bement, W.M.,
618 2009. Action at a distance during cytokinesis. J. Cell Biol. 187, 831–845.
619 doi:10.1083/jcb.200907090.dv
620 de-Carvalho, J., Deshpande, O., Nabais, C., Telley, I.A., 2018. A cell-free system of Drosophila
621 egg explants supporting native mitotic cycles. Methods Cell Biol. 144, 233–257.
622 doi:10.1016/bs.mcb.2018.03.011
623 Deneke, V.E., Puliafito, A., Krueger, D., Narla, A.V., De Simone, A., Primo, L., Vergassola, M.,
624 De Renzis, S., Di Talia, S., 2019. Self-Organized Nuclear Positioning Synchronizes the Cell
625 Cycle in Drosophila Embryos. Cell 177, 925–941.e17. doi:10.1016/j.cell.2019.03.007
626 Dickinson, D.J., Nelson, W.J., Weis, W.I., 2012. An epithelial tissue in Dictyostelium challenges
627 the traditional origin of metazoan multicellularity. Bioessays 34, 833–840.
628 doi:10.1002/bies.201100187
629 Dudin, O., Ondracka, A., Grau-Bové, X., Haraldsen, A.A., Toyoda, A., Suga, H., Bråte, J., Ruiz-
630 Trillo, I., 2019. A unicellular relative of animals generates a layer of polarized cells by
631 actomyosin-dependent cellularization. Elife 8, 3123. doi:10.7554/eLife.49801
632 D'Avino, P.P., Archambault, V., Przewloka, M.R., Zhang, W., Lilley, K.S., Laue, E., Glover,
633 D.M., 2007. Recruitment of Polo kinase to the spindle midzone during cytokinesis requires
634 the Feo/Klp3A complex. PLoS ONE 2, e572. doi:10.1371/journal.pone.0000572
635 Foe, V.E., Alberts, B.M., 1983. Studies of nuclear and cytoplasmic behaviour during the five
636 mitotic cycles that precede gastrulation in Drosophila embryogenesis. Journal of Cell Science
637 61, 31–70.
638 Forth, S., Hsia, K.-C., Shimamoto, Y., Kapoor, T.M., 2014. Asymmetric friction of nonmotor
639 MAPs can lead to their directional motion in active microtubule networks. Cell 157, 420–
640 432. doi:10.1016/j.cell.2014.02.018
641 Fu, C., Ward, J.J., Loiodice, I., Velve-Casquillas, G., Nédélec, F.J., Tran, P.T., 2009. Phospho-
642 regulated interaction between kinesin-6 Klp9p and microtubule bundler Ase1p promotes
643 spindle elongation. Dev. Cell 17, 257–267. doi:10.1016/j.devcel.2009.06.012
644 Gibeaux, R., Politi, A.Z., Philippsen, P., Nedelec, F., 2017. Mechanism of nuclear movements in
645 a multinucleated cell. Mol. Biol. Cell 28, 645–660. doi:10.1091/mbc.E16-11-0806
646 Gundersen, G.G., Worman, H.J., 2013. Nuclear positioning. Cell 152, 1376–1389.
647 doi:10.1016/j.cell.2013.02.031
648 Hatanaka, K., Okada, M., 1991. Retarded nuclear migration in Drosophila embryos with aberrant
649 F-actin reorganization caused by maternal mutations and by cytochalasin treatment.
650 Development 111, 909–920.
651 Heck, M.M., Pereira, A., Pesavento, P., Yannoni, Y., Spradling, A.C., Goldstein, L.S., 1993. The
652 kinesin-like protein KLP61F is essential for mitosis in Drosophila. J. Cell Biol. 123, 665–
653 679. doi:10.1083/jcb.123.3.665
654 Hehenberger, E., Kradolfer, D., Köhler, C., 2012. Endosperm cellularization defines an important
655 developmental transition for embryo development. Development 139, 2031–2039.
656 doi:10.1242/dev.077057
657 Howard, J., 2001. Mechanics of Motor Proteins and the Cytoskeleton. Sinauer Associates
658 Incorporated.

659 Hu, C.-K., Ozlü, N., Coughlin, M., Steen, J.J., Mitchison, T.J., 2012. Plk1 negatively regulates
660 PRC1 to prevent premature midzone formation before cytokinesis. Mol. Biol. Cell 23, 2702–
661 2711. doi:10.1091/mbc.E12-01-0058
662 Hyman, A.A., 1991. Preparation of marked microtubules for the assay of the polarity of
663 microtubule-based motors by fluorescence. J. Cell Sci. Suppl. 14, 125–127.
664 doi:10.1242/jcs.1991.supplement_14.25
665 Kanesaki, T., Edwards, C.M., Schwarz, U.S., Grosshans, J., 2011. Dynamic ordering of nuclei in
666 syncytial embryos: a quantitative analysis of the role of cytoskeletal networks. Integr. Biol. 3,
667 1112–1119. doi:10.1039/c1ib00059d
668 Kao, L.-R., Megraw, T.L., 2009. Centrocortin cooperates with centrosomin to organize
669 Drosophila embryonic cleavage furrows. Curr. Biol. 19, 937–942.
670 doi:10.1016/j.cub.2009.04.037
671 Kapitein, L.C., Peterman, E.J.G., Kwok, B.H., Kim, J.H., Kapoor, T.M., Schmidt, C.F., 2005.
672 The bipolar mitotic kinesin Eg5 moves on both microtubules that it crosslinks. Nature 435,
673 114–118. doi:10.1038/nature03503
674 Karr, T.L., Alberts, B.M., 1986. Organization of the cytoskeleton in early Drosophila embryos. J.
675 Cell Biol. 102, 1494–1509.
676 Kellogg, D.R., Mitchison, T.J., Alberts, B.M., 1988. Behaviour of microtubules and actin
677 filaments in living Drosophila embryos. Development 103, 675–686.
678 Kellogg, E.H., Howes, S., Ti, S.-C., Ramírez-Aportela, E., Kapoor, T.M., Chacón, P., Nogales,
679 E., 2016. Near-atomic cryo-EM structure of PRC1 bound to the microtubule. Proc. Natl.
680 Acad. Sci. U.S.A. 113, 9430–9439. doi:10.1073/pnas.1609903113
681 Khmelinskii, A., Roostalu, J., Roque, H., Antony, C., Schiebel, E., 2009. Phosphorylation-
682 dependent protein interactions at the spindle midzone mediate cell cycle regulation of spindle
683 elongation. Dev. Cell 17, 244–256. doi:10.1016/j.devcel.2009.06.011
684 Kotadia, S., Crest, J., Tram, U., Riggs, B., Sullivan, W., 2001. Blastoderm Formation and
685 Cellularisation in Drosophila melanogaster. American Cancer Society, Chichester, UK.
686 doi:10.1002/9780470015902.a0001071.pub2
687 Kurasawa, Y., Earnshaw, W.C., Mochizuki, Y., Dohmae, N., Todokoro, K., 2004. Essential roles
688 of KIF4 and its binding partner PRC1 in organized central spindle midzone formation.
689 EMBO J. 23, 3237–3248. doi:10.1038/sj.emboj.7600347
690 Kwon, M., Morales-Mulia, S., Brust-Mascher, I., Rogers, G.C., Sharp, D.J., Scholey, J.M., 2004.
691 The chromokinesin, KLP3A, dives mitotic spindle pole separation during prometaphase and
692 anaphase and facilitates chromatid motility. Mol. Biol. Cell 15, 219–233.
693 doi:10.1091/mbc.E03-07-0489
694 Kwon, M., Scholey, J.M., 2004. Spindle mechanics and dynamics during mitosis in Drosophila.
695 Trends in Cell Biology 14, 194–205. doi:10.1016/j.tcb.2004.03.003
696 Lecuit, T., 2004. Junctions and vesicular trafficking during Drosophila cellularization. Journal of
697 Cell Science 117, 3427–3433. doi:10.1242/jcs.01312
698 Lecuit, T., Wieschaus, E., 2000. Polarized insertion of new membrane from a cytoplasmic
699 reservoir during cleavage of the Drosophila embryo. J. Cell Biol. 150, 849–860.
700 doi:10.1083/jcb.150.4.849
701 Lele, T.P., Dickinson, R.B., Gundersen, G.G., 2018. Mechanical principles of nuclear shaping
702 and positioning. J. Cell Biol. 217, 3330–3342. doi:10.1083/jcb.201804052

703 Levy, J.R., Holzbaur, E.L.F., 2008. Dynein drives nuclear rotation during forward progression of
704 motile fibroblasts. Journal of Cell Science 121, 3187–3195. doi:10.1242/jcs.033878
705 Lv, Z., Rosenbaum, J., Mohr, S., Zhang, X., Kong, D., Preiß, H., Kruss, S., Alim, K.,
706 Aspelmeier, T., Grosshans, J., 2020. The Emergent Yo-yo Movement of Nuclei Driven by
707 Cytoskeletal Remodeling in Pseudo-synchronous Mitotic Cycles. Curr. Biol.
708 doi:10.1016/j.cub.2020.04.078
709 Manhart, A., Windner, S., Baylies, M., Mogilner, A., 2018. Mechanical positioning of multiple
710 nuclei in muscle cells. PLoS Comput. Biol. 14, e1006208. doi:10.1371/journal.pcbi.1006208
711 Markow, T.A., Beall, S., Matzkin, L.M., 2008. Egg size, embryonic development time and
712 ovoviviparity in Drosophila species. Journal of Evolutionary Biology 22, 430–434.
713 doi:10.1111/j.1420-9101.2008.01649.x
714 Mavrakis, M., Rikhy, R., Lippincott-Schwartz, J., 2009a. Plasma membrane polarity and
715 compartmentalization are established before cellularization in the fly embryo. Dev. Cell 16,
716 93–104. doi:10.1016/j.devcel.2008.11.003
717 Mavrakis, M., Rikhy, R., Lippincott-Schwartz, J., 2009b. Cells within a cell: Insights into cellular
718 architecture and polarization from the organization of the early fly embryo. Commun Integr
719 Biol 2, 313–314.
720 Megraw, T.L., Li, K., Kao, L.R., Kaufman, T.C., 1999. The centrosomin protein is required for
721 centrosome assembly and function during cleavage in Drosophila. Development 126, 2829–
722 2839.
723 Minc, N., Burgess, D., Chang, F., 2011. Influence of cell geometry on division-plane positioning.
724 Cell 144, 414–426. doi:10.1016/j.cell.2011.01.016
725 Morin, X., Daneman, R., Zavortink, M., Chia, W., 2001. A protein trap strategy to detect GFP-
726 tagged proteins expressed from their endogenous loci in Drosophila. Proc. Natl. Acad. Sci.
727 U.S.A. 98, 15050–15055. doi:10.1073/pnas.261408198
728 Neelam, S., Chancellor, T.J., Li, Y., Nickerson, J.A., Roux, K.J., Dickinson, R.B., Lele, T.P.,
729 2015. Direct force probe reveals the mechanics of nuclear homeostasis in the mammalian
730 cell. Proc. Natl. Acad. Sci. U.S.A. 112, 5720–5725. doi:10.1073/pnas.1502111112
731 Nguyen, P.A., Groen, A.C., Loose, M., Ishihara, K., Wühr, M., Field, C.M., Mitchison, T.J.,
732 2014. Spatial organization of cytokinesis signaling reconstituted in a cell-free system.
733 Science 346, 244–247. doi:10.1126/science.1256773
734 Page, S.L., Hawley, R.S., 2005. The Drosophila meiotic mutant mei-352 is an allele of klp3A and
735 reveals a role for a kinesin-like protein in crossover distribution. Genetics 170, 1797–1807.
736 doi:10.1534/genetics.105.041194
737 Pecreaux, J., Redemann, S., Alayan, Z., Mercat, B., Pastezeur, S., Garzon-Coral, C., Hyman,
738 A.A., Howard, J., 2016. The Mitotic Spindle in the One-Cell C. elegans Embryo Is
739 Positioned with High Precision and Stability. Biophys. J. 111, 1773–1784.
740 doi:10.1016/j.bpj.2016.09.007
741 Perkins, L.A., Holderbaum, L., Tao, R., Hu, Y., Sopko, R., McCall, K., Yang-Zhou, D.,
742 Flockhart, I., Binari, R., Shim, H.-S., Miller, A., Housden, A., Foos, M., Randkelv, S.,
743 Kelley, C., Namgyal, P., Villalta, C., Liu, L.-P., Jiang, X., Huan-Huan, Q., Wang, X.,
744 Fujiyama, A., Toyoda, A., Ayers, K., Blum, A., Czech, B., Neumuller, R., Yan, D.,
745 Cavallaro, A., Hibbard, K., Hall, D., Cooley, L., Hannon, G.J., Lehmann, R., Parks, A.,
746 Mohr, S.E., Ueda, R., Kondo, S., Ni, J.-Q., Perrimon, N., 2015. The Transgenic RNAi

747 Project at Harvard Medical School: Resources and Validation. Genetics 201, 843–852.
748 doi:10.1534/genetics.115.180208
749 Petkova, M.D., Tkačik, G., Bialek, W., Wieschaus, E.F., Gregor, T., 2019. Optimal Decoding of
750 Cellular Identities in a Genetic Network. Cell 176, 844–855.e15.
751 doi:10.1016/j.cell.2019.01.007
752 Polak, B., Risteski, P., Lesjak, S., Tolić, I.M., 2017. PRC1-labeled microtubule bundles and
753 kinetochore pairs show one-to-one association in metaphase. EMBO Rep. 18, 217–230.
754 doi:10.15252/embr.201642650
755 Postner, M.A., Miller, K.G., Wieschaus, E.F., Wieschaus, E.F., 1992. Maternal effect mutations
756 of the sponge locus affect actin cytoskeletal rearrangements in Drosophila melanogaster
757 embryos. J. Cell Biol. 119, 1205–1218.
758 Reinemann, D.N., Sturgill, E.G., Das, D.K., Degen, M.S., Vörös, Z., Hwang, W., Ohi, R., Lang,
759 M.J., 2017. Collective Force Regulation in Anti-parallel Microtubule Gliding by Dimeric
760 Kif15 Kinesin Motors. Curr. Biol. 27, 2810–2820.e6. doi:10.1016/j.cub.2017.08.018
761 Royou, A., Field, C., Sisson, J.C., Sullivan, W., Karess, R., 2004. Reassessing the role and
762 dynamics of nonmuscle myosin II during furrow formation in early Drosophila embryos.
763 Mol. Biol. Cell 15, 838–850. doi:10.1091/mbc.E03-06-0440
764 Sarov, M., Barz, C., Jambor, H., Hein, M.Y., Schmied, C., Suchold, D., Stender, B., Janosch, S.,
765 K J, V.V., Krishnan, R.T., Krishnamoorthy, A., Ferreira, I.R.S., Ejsmont, R.K., Finkl, K.,
766 Hasse, S., Kämpfer, P., Plewka, N., Vinis, E., Schloissnig, S., Knust, E., Hartenstein, V.,
767 Mann, M., Ramaswami, M., VijayRaghavan, K., Tomancak, P., Schnorrer, F., 2016. A
768 genome-wide resource for the analysis of protein localisation in Drosophila. Elife 5, e12068.
769 doi:10.7554/eLife.12068
770 Sasabe, M., Machida, Y., 2006. MAP65: a bridge linking a MAP kinase to microtubule turnover.
771 Current Opinion in Plant Biology 9, 563–570. doi:10.1016/j.pbi.2006.09.010
772 Sawin, K.E., LeGuellec, K., Philippe, M., Mitchison, T.J., 1992. Mitotic spindle organization by
773 a plus-end-directed microtubule motor. Nature 359, 540–543. doi:10.1038/359540a0
774 Schindelin, J., Arganda-Carreras, I., Frise, E., Kaynig, V., Longair, M., Pietzsch, T., Preibisch,
775 S., Rueden, C., Saalfeld, S., Schmid, B., Tinevez, J.-Y., White, D.J., Hartenstein, V., Eliceiri,
776 K., Tomancak, P., Cardona, A., 2012. Fiji: an open-source platform for biological-image
777 analysis. Nat Meth 9, 676–682. doi:10.1038/nmeth.2019
778 Scholey, J.M., Civelekoglu-Scholey, G., Brust-Mascher, I., 2016. Anaphase B. Biology (Basel) 5,
779 51. doi:10.3390/biology5040051
780 Schuh, M., Schuh, M., Lehner, C.F., Heidmann, S., 2007. Incorporation of Drosophila
781 CID/CENP-A and CENP-C into centromeres during early embryonic anaphase. Current
782 Biology 17, 237–243. doi:10.1016/j.cub.2006.11.051
783 Schuyler, S.C., Liu, J.Y., Pellman, D., 2003. The molecular function of Ase1p: evidence for a
784 MAP-dependent midzone-specific spindle matrix. Microtubule-associated proteins. J. Cell
785 Biol. 160, 517–528. doi:10.1083/jcb.200210021
786 Sharp, D.J., Yu, K.R., Sisson, J.C., Sullivan, W., Scholey, J.M., 1999. Antagonistic microtubule-
787 sliding motors position mitotic centrosomes in Drosophila early embryos. Nature Cell
788 Biology 1, 51–54. doi:10.1038/9025
789 Staller, M.V., Yan, D., Randklev, S., Bragdon, M.D., Wunderlich, Z.B., Tao, R., Perkins, L.A.,
790 Depace, A.H., Perrimon, N., 2013. Depleting gene activities in early Drosophila embryos

791 with the “maternal-Gal4-shRNA” system. Genetics 193, 51–61.
792 doi:10.1534/genetics.112.144915
793 Starr, D.A., Han, M., 2002. Role of ANC-1 in tethering nuclei to the actin cytoskeleton. Science
794 298, 406–409. doi:10.1126/science.1075119
795 Stocker, H., Gallant, P., 2008. Getting started : an overview on raising and handling Drosophila.
796 Methods Mol. Biol. 420, 27–44. doi:10.1007/978-1-59745-583-1_2
797 Subramanian, R., Ti, S.-C., Tan, L., Darst, S.A., Kapoor, T.M., 2013. Marking and measuring
798 single microtubules by PRC1 and kinesin-4. Cell 154, 377–390.
799 doi:10.1016/j.cell.2013.06.021
800 Subramanian, R., Wilson-Kubalek, E.M., Arthur, C.P., Bick, M.J., Campbell, E.A., Darst, S.A.,
801 Milligan, R.A., Kapoor, T.M., 2010. Insights into antiparallel microtubule crosslinking by
802 PRC1, a conserved nonmotor microtubule binding protein. Cell 142, 433–443.
803 doi:10.1016/j.cell.2010.07.012
804 Tao, L., Mogilner, A., Civelekoglu-Scholey, G., Wollman, R., Evans, J., Stahlberg, H., Scholey,
805 J.M., 2006. A homotetrameric kinesin-5, KLP61F, bundles microtubules and antagonizes
806 Ncd in motility assays. Current Biology 16, 2293–2302. doi:10.1016/j.cub.2006.09.064
807 Telley, I.A., Gáspár, I., Ephrussi, A., Surrey, T., 2013. A single Drosophila embryo extract for
808 the study of mitosis ex vivo. Nat Protoc 8, 310–324. doi:10.1038/nprot.2013.003
809 Telley, I.A., Gáspár, I., Ephrussi, A., Surrey, T., 2012. Aster migration determines the length
810 scale of nuclear separation in the Drosophila syncytial embryo. J. Cell Biol. 197, 887–895.
811 doi:10.1083/jcb.201204019
812 Vaizel-Ohayon, D., Schejter, E.D., 1999. Mutations in centrosomin reveal requirements for
813 centrosomal function during early Drosophila embryogenesis. Current Biology 9, 889–898.
814 Vernì, F., Somma, M.P., Gunsalus, K.C., Bonaccorsi, S., Belloni, G., Goldberg, M.L., Gatti, M.,
815 2004. Feo, the Drosophila homolog of PRC1, is required for central-spindle formation and
816 cytokinesis. Current Biology 14, 1569–1575. doi:10.1016/j.cub.2004.08.054
817 Wang, H., Brust-Mascher, I., Scholey, J.M., 2015. The microtubule cross-linker Feo controls the
818 midzone stability, motor composition, and elongation of the anaphase B spindle in
819 Drosophila embryos. Mol. Biol. Cell 26, 1452–1462. doi:10.1091/mbc.E14-12-1631
820 Wheatley, S., Kulkarni, S., Karess, R., 1995. Drosophila nonmuscle myosin II is required for
821 rapid cytoplasmic transport during oogenesis and for axial nuclear migration in early
822 embryos. Development 121, 1937–1946.
823 Wijeratne, S., Subramanian, R., 2018. Geometry of antiparallel microtubule bundles regulates
824 relative sliding and stalling by PRC1 and Kif4A. Elife 7, 37782. doi:10.7554/eLife.32595
825 Williams, B.C., Dernburg, A.F., Puro, J., Nokkala, S., Goldberg, M.L., 1997. The Drosophila
826 kinesin-like protein KLP3A is required for proper behavior of male and female pronuclei at
827 fertilization. Development 124, 2365–2376.
828 Williams, B.C., Riedy, M.F., Williams, E.V., Gatti, M., Goldberg, M.L., 1995. The Drosophila
829 kinesin-like protein KLP3A is a midbody component required for central spindle assembly
830 and initiation of cytokinesis. J. Cell Biol. 129, 709–723. doi:10.1083/jcb.129.3.709
831 Wühr, M., Dumont, S., Groen, A.C., Needleman, D.J., Mitchison, T.J., 2009. How does a
832 millimeter-sized cell find its center? cc 8, 1115–1121. doi:10.4161/cc.8.8.8150

833 Zhu, C., Lau, E., Schwarzenbacher, R., Bossy-Wetzel, E., Jiang, W., 2006. Spatiotemporal
834 control of spindle midzone formation by PRC1 in human cells. Proc. Natl. Acad. Sci. U.S.A.
835 103, 6196–6201. doi:10.1073/pnas.0506926103
836

837 Acknowledgements

838 We thank members of the Telley lab for fruitful discussions, Jonathon Scholey for constructive
839 comments on the manuscript and for fly stocks, and Thomas Surrey for discussions throughout the
840 project. We thank the staff of the Fly Facility, the Advanced Imaging Facility and the Technical
841 Support Service at the Instituto Gulbenkian de Ciência (IGC). Transgenic fly stocks were obtained
842 from the Vienna Drosophila Resource Center and Bloomington Drosophila Stock Center (NIH
843 P40OD018537). We acknowledge financial support provided by Fundação Calouste Gulbenkian
844 (FCG), European Commission FP7 Marie Curie CIG to I.A.T. (PCIG13-GA-2013-618743),
845 Human Frontiers Science Program YIG to I.A.T. (RGY0083/2016), a doctoral fellowship
846 SFRH/BD/52174/2013 to O.D. from Fundação para a Ciência e a Tecnologia (FCT). We
847 acknowledge LISBOA-01-0145-FEDER-007654 supporting IGC's core operation, LISBOA-01-
848 0145-FEDER-022170 (*Congento*) supporting the Fly Facility, and PPBI-POCI-01-0145-FEDER-
849 022122 supporting the Advanced Imaging Facility, all co-financed by FCT (Portugal) and
850 Lisboa2020, under the PORTUGAL2020 agreement (European Regional Development Fund).

851 Author contributions

852 OD, JC and IAT conceived and designed the project. OD and IAT designed experiments and OD
853 performed them with occasional support from JC. DMV and OD designed, purified and
854 characterized the protein constructs. IAT designed and assembled the instrument for explant
855 generation and manipulation. OD and IAT prepared the figures and wrote the manuscript.

856 Declaration of interests

857 The authors declare no competing interests.

858 Web resources

859 A Database of Drosophila Genes & Genomes, http://flybase.org/.

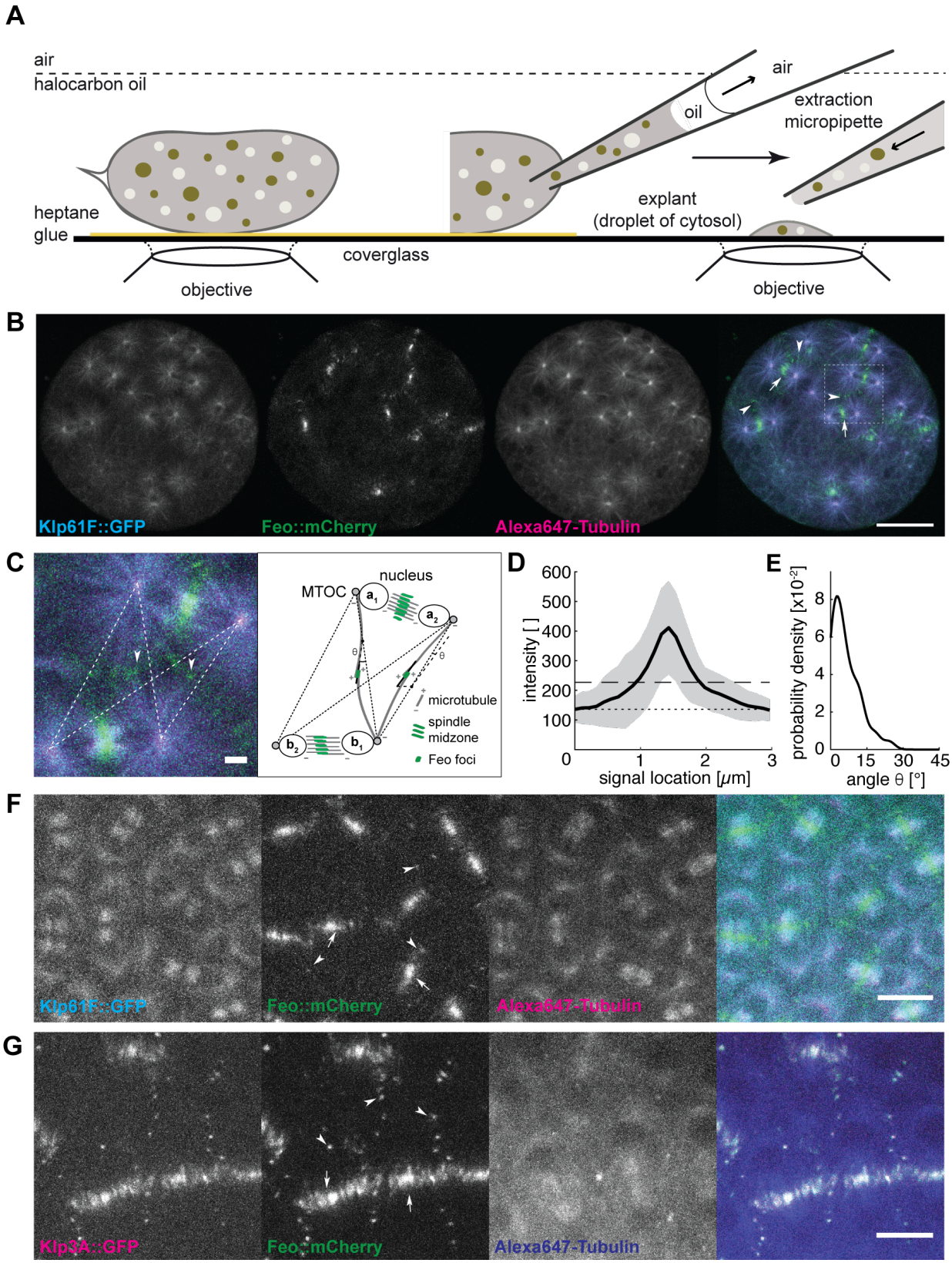

Figure 1: Feo, Klp3A and Klp61F localization confirm antiparallel microtubule overlaps between asters of non-sister nuclei.

A) Schematic showing a *Drosophila* syncytial embryo immobilized to the coverslip and covered with a thin layer of halocarbon oil ready for time-lapse microscopy. On the right, a preblastoderm

embryo is punctured for extraction and deposition of cytosol on the coverslip using a micropipette, thereby generating a series of embryo explants. **B)** Three-color snapshot from a time-lapse (Suppl. Video 1) of an explant generated from an embryo expressing Klp61F::GFP (cyan), Feo::mCherry (green) and injected with Alexa647–Tubulin (magenta). During the anaphase/telophase transition, Feo strongly localized to the spindle midzone (arrows) and to the intercalating microtubules from neighboring nuclei (arrowheads). Scale bar, 30 µm. **C)** Zoom-in of the merged color channel image in b) (dashed square). Feo localized as intense foci between neighboring spindles, where microtubules from non-sister nuclei meet (arrowheads show examples). The schematic on the right represents the configuration shown in the image, exemplifying the location of the two pairs of sister nuclei, a^1–a^2 and b^1–b^2, and two representative Feo foci. The dashed lines represent the shortest path of microtubule interactions between the MTOCs of non-sister nuclei. An intensity profile of the foci was generated by drawing a line (continuous) along the longest axis and centered to the foci. The angle θ relative to the dashed interaction line was determined. Scale bar, 2 µm. **D)** The average intensity profile of Feo foci indicate a foci length of 1.0±0.35 µm. The grey area designates the standard deviation (SD), the dotted line marks the background level, and the dashed line marks two times SD above the background. N=7; n=57. **E)** The distribution of angles (θ) suggests that the antiparallel microtubule overlaps occur mostly along the connecting line between the neighboring non-sister nuclei. N=7; n=42. Cases where foci were symmetric, and a long axis could not be determined were excluded from the analysis. **F)** Three-color snapshot of a blastoderm embryo expressing Klp61F::GFP (cyan), Feo::mCherry (green) and injected with Alexa647–Tubulin (magenta) showed that Feo localized strongly between sister nuclei as part of the spindle midzone (arrows) and, more strikingly, between neighboring non-sister nuclei as distinct foci (arrowheads). Scale bar, 10 µm. Refer to Suppl. Video 2. **G)** Three-color snapshot of a blastoderm embryo expressing Klp3A::GFP (magenta), Feo::mCherry (green) and injected with Alexa647–Tubulin (blue) showed that Klp3A co-localizes with Feo at the spindle midzone (arrows) and at the foci between neighboring non-sister nuclei (arrowheads). Scale bar, 10 µm. Refer to Suppl. Video 3.

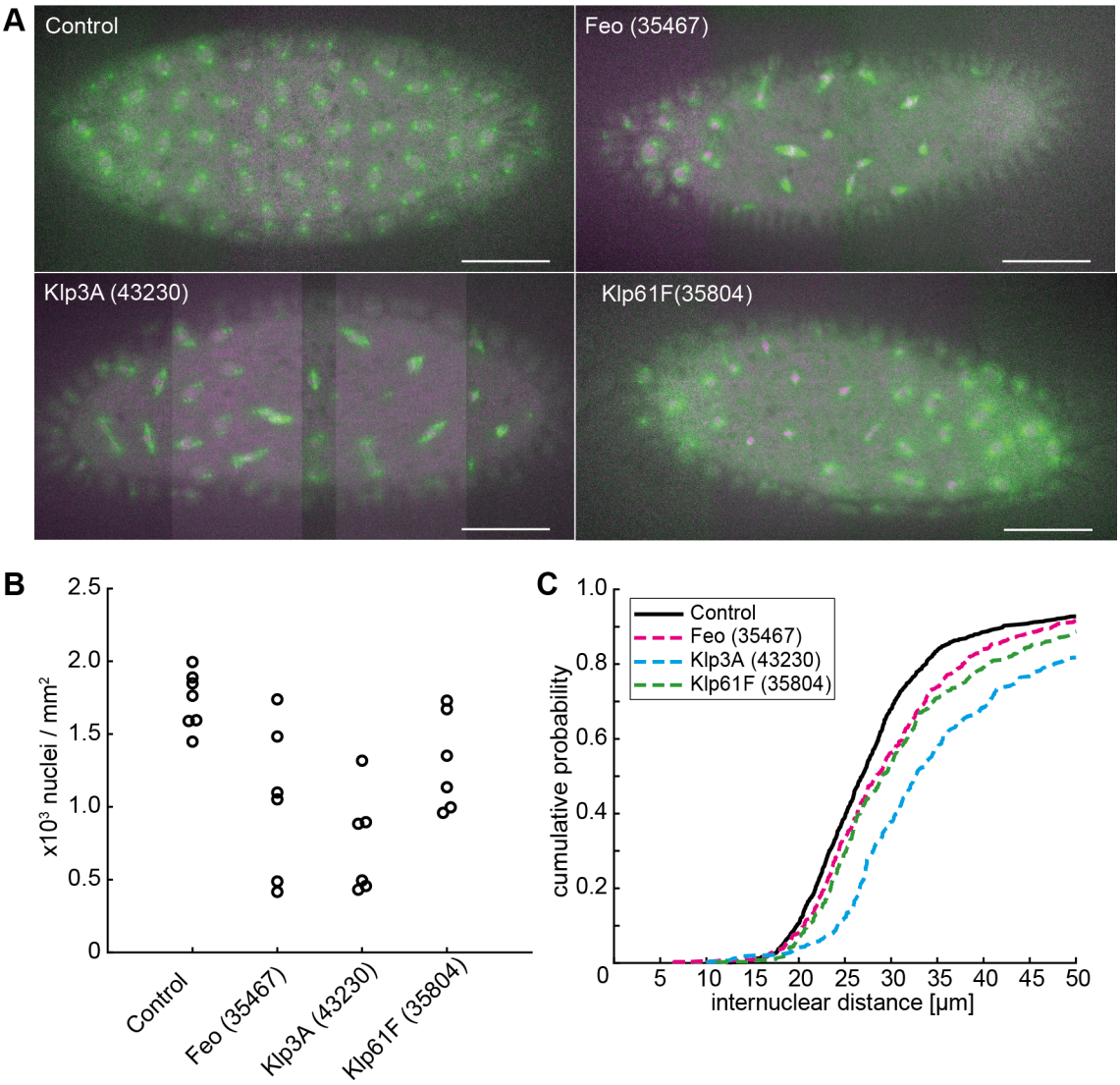

Figure 2: Partial knockdown of Feo, Klp3a or Klp61F by RNAi leads to defective nuclear delivery to the embryo cortex.

A) Maximum intensity projections from three-dimensional time-lapse movies of embryos partially depleted of Feo, Klp3A or Klp61F, expressing Jupiter::GFP (green) marking microtubules and H2Av::RFP (magenta) marking chromatin. Knockdown embryos showed irregular nuclear distribution during the first interphase occurring at the cortex as compared to the regular nuclear distribution in control embryos (RNAi against mCherry). Scale bar, 50 µm. **B)** A quantification of the number of nuclei per square millimeter showed a higher degree of variation between the six embryos knocked down for either of the three genes Feo (35467), Klp3A (40230) or Klp61F (35804) as compared with control embryos. In all cases, the density decreased on average. Each data point represents one embryo. **C)** The cumulative probability function of the internuclear distance between first-order neighbors in embryos depleted of Feo, Klp3A or Klp61F showed on average a higher internuclear distance. Thus, the number of nuclei at the cortex was smaller with broader distribution indicating greater irregularity with respect to the control. N=7 (control), N=6 (RNAi lines). Refer to Suppl. Fig. 2 and Video 4.

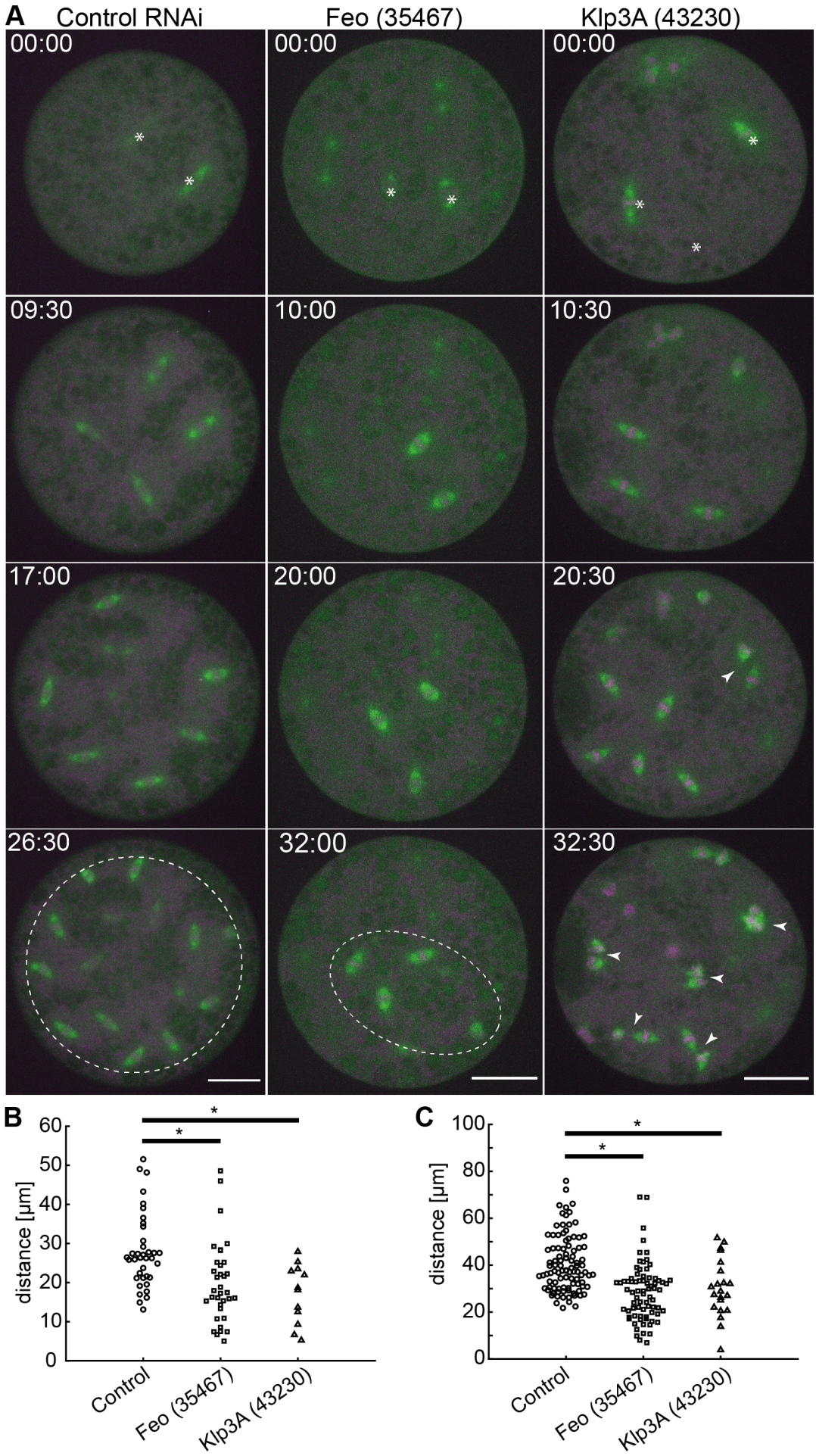
A
Control RNAi
Feo (35467)
Klp3A (43230)
00:00
00:00
00:00
09:30
10:00
10:30
17:00
20:00
20:30
26:30
32:00
32:30
B
distance [µm]
60
50
40
30
20
10
0
*
*
Control
Feo (35467)
Klp3A (43230)
C
distance [µm]
100
80
60
40
20
0
*
*
Control
Feo (35467)
Klp3A (43230)

908

909 **Figure 3: Partial knockdown of Feo, Klp3a or Klp61F by RNAi leads to defective nuclear**
910 **distribution in preblastoderm embryo explants.**

911 **A)** Maximum intensity projections from time-lapse movies of embryo explants under control
912 conditions and partial depletion of Feo, Klp3A or Klp61F, while expressing Jupiter::GFP (green)
913 marking microtubules and H2Av::RFP (magenta) marking chromatin. Each panel shows
914 metaphase of consecutive division. White stars in the first frame mark the position of dividing
915 nuclei (sometimes out of focus). The control explants (RNAi against mCherry) underwent normal
916 nuclear divisions and distributed the daughter nuclei within the entire explant volume (dashed
917 circle). Explants from Feo depleted embryos underwent mitotic nuclear divisions but daughter
918 nuclei separate less efficiently, leading to a partial occupation of the cytoplasm (dashed ellipse).
919 Explants from Klp3A depleted embryos underwent mitotic nuclear divisions with slightly less
920 efficient distribution than in controls and with higher prevalence for spindle fusion (arrowheads).
921 Scale bar, 30 µm; time in min:sec. **B)** Separation distance between daughter nuclei after mitotic
922 nuclear division under control conditions and under knockdown for Feo (35467) and Klp3A
923 (43230) in embryo explants. Separation distance was significantly reduced in both knock-down
924 conditions (Control: N=4, n=38; Feo (35467): N=2, n=36; Klp3A (43230): N=3, n=23; $p<0.01$,
925 Wilcoxon signed-rank test). **C)** Separation distance between first-neighbor non-sibling nuclei
926 measured between mitotic divisions under control conditions and under knockdown for Feo
927 (35467) and Klp3A (43230) in embryo explants. The separation distance was significantly shorter
928 in both knockdown conditions (Control: N=3, n=98; Feo (35467): N=3, n=77; Klp3A (43230):
929 N=3, n=50; $p<0.05$, Wilcoxon signed-rank test) though the effect is stronger when Feo is depleted.

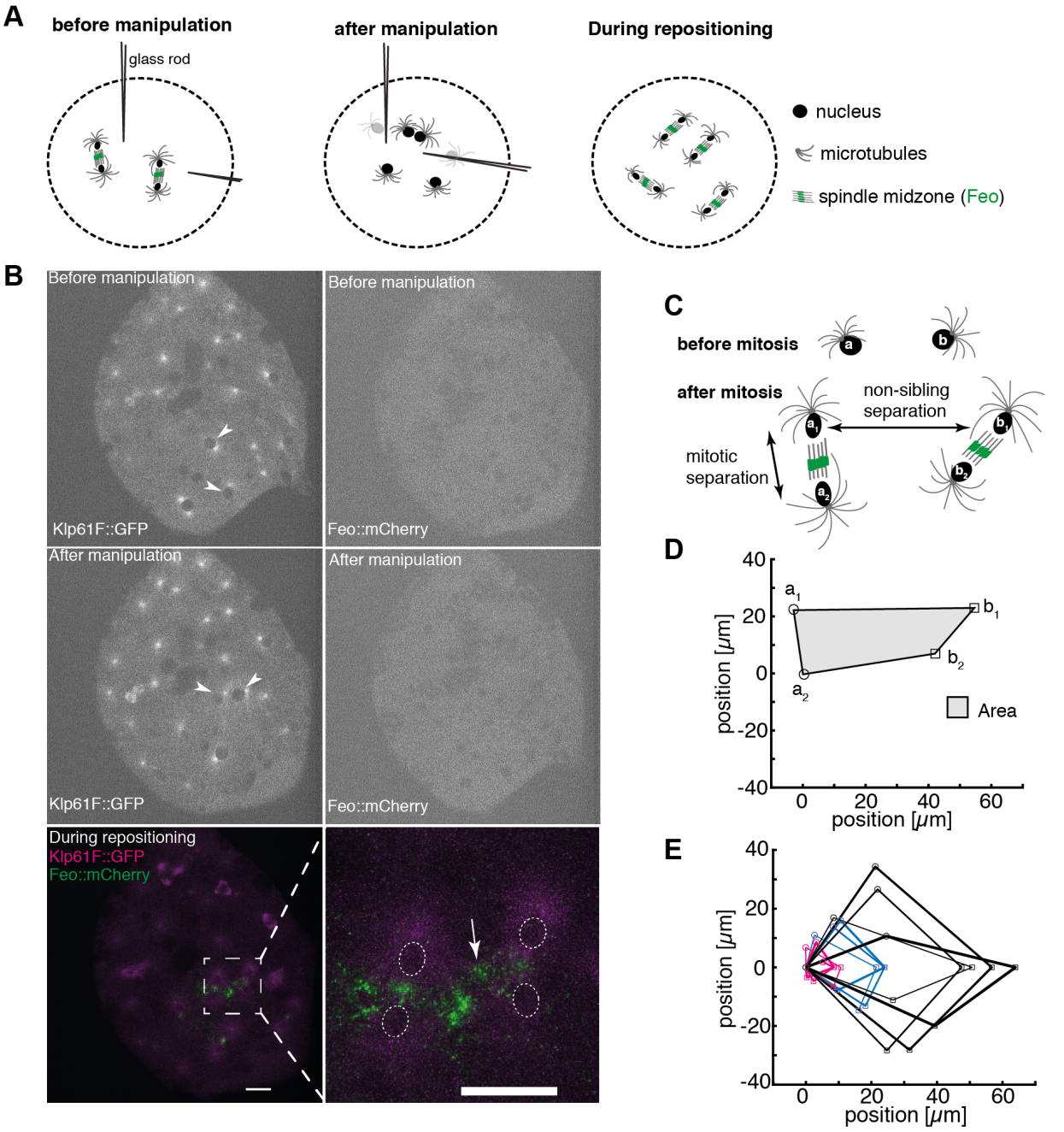
A
before manipulation
glass rod
after manipulation
During repositioning
nucleus
microtubules
spindle midzone (Feo)
B
Before manipulation
Klp61F::GFP
Before manipulation
Feo::mCherry
After manipulation
Klp61F::GFP
After manipulation
Feo::mCherry
During repositioning
Klp61F::GFP
Feo::mCherry
C
before mitosis
after mitosis
non-sibling separation
mitotic separation
D
position [μm]
Area
E
position [μm]

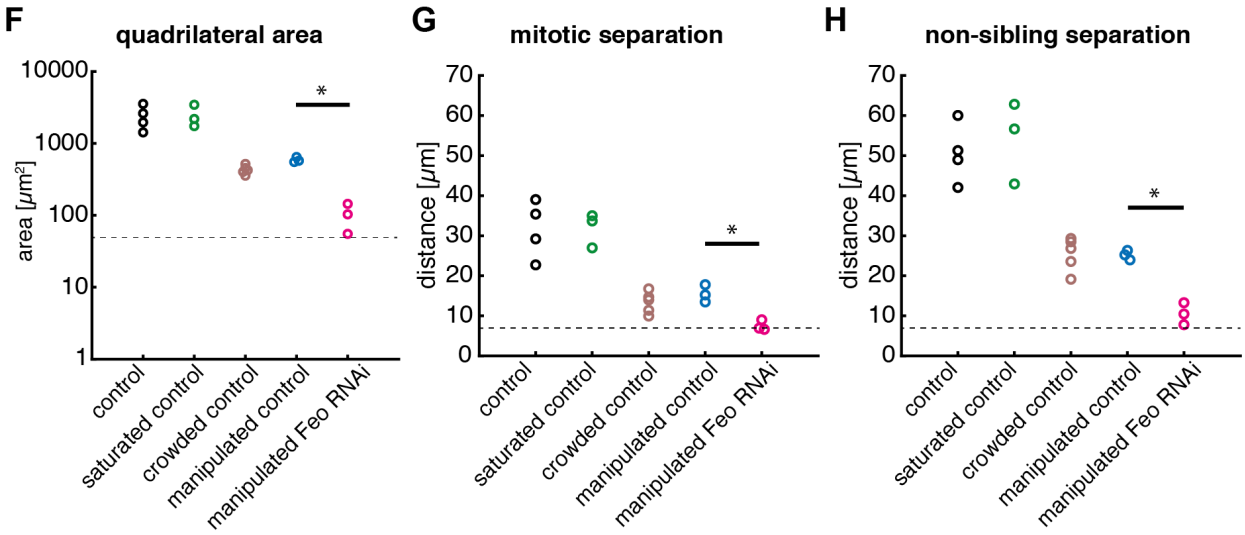
F
quadrilateral area
area [μm²]
G
mitotic separation
distance [μm]
H
non-sibling separation
distance [μm]
control
saturated control
crowded control
manipulated control
manipulated Feo RNAi

930

Figure 4: Feo depleted explants fail to maintain nuclear separation distance following acute physical manipulation.

A) Scheme showing the manipulation of internuclear distance in embryo explants. After a mitotic division and nuclear separation, two non-sister nuclei were brought close to each other during anaphase B–telophase by means of two glass rods. Subsequently, nuclei divided again, and daughter nuclei separated at defined distances. **B)** Fluorescence images illustrating physical manipulation of nuclear position in an explant made from an embryo expressing Klp61F::GFP (green) marking microtubules positively and nuclei negatively due to exclusion (dark disks), together with Feo::mCherry (magenta). The top two rows show the GFP and mCherry signal before (left) and after (right) manipulation. Physical manipulation decreased the distance selectively between two nuclei (arrowheads). Scale bar, 30 µm. Upon conclusion of the next mitosis and during repositioning of the daughter nuclei (bottom), Feo localized exclusively between the daughters of manipulated nuclei (zoom on the right), indicating that microtubule overlaps have formed. In contrast, Feo localization is not detectable between manipulated nucleus before or immediately after manipulation or between nuclei that have not been moved and are further apart. Scale bars, 15 µm. **C)** Schematic of the mitotic separation distance and non-sister separation distance. Nuclei a and b were brought close to each other and following a division give rise to daughters a_1, a_2, and b_1, b_2, respectively. **D)** Schematic of the quadrilateral area defined by the four nuclei a_1, a_2, b_1, b_2 after mitosis as shown in c). **E)** Overlay of quadrilaterals aligned for coordinate $\mathbf{a_2}$ and rotated so that the vector $\mathbf{b_1}$–$\mathbf{a_2}$ matches the *x*-axis. Control RNAi experiments without manipulation and with ample space in the explant are in black (N=4), experiments involving manipulation under control RNAi conditions are shown in blue (N=3), and manipulations experiments under knockdown of Feo are shown in magenta (N=3). The quadrilateral area for nuclei manipulated in Feo depleted explants was smaller when compared with control. **F)** Quadrilateral area for five different experimental conditions. The same color code as in E applies; additional control conditions without manipulation in explants almost saturated with nuclei (N=3) and in explants crowded with nuclei (N=5) are shown in green and brown, respectively. The dashed line designates the lower boundary where the four nuclei touch each other. The quadrilateral area for nuclei manipulated in Feo depleted explants was smaller when compared with control. **G)** The average mitotic separation distance between the dividing nuclei ($|\mathbf{a_1}–\mathbf{a_2}|$; $|\mathbf{b_1}–\mathbf{b_2}|$) was reduced in the manipulated Feo RNAi condition and was close to the lower limit of separation (nuclear diameter) where the nuclei are touching each other. In contrast, sister nuclei were separated in all the control conditions. The color code is the same as in **F**. **H)** The average non-sister separation between the dividing nuclei ($|\mathbf{a_1}–\mathbf{b_1}|$; $|\mathbf{a_2}–\mathbf{b_2}|$) was reduced in the manipulated Feo RNAi condition and was close to the lower limit of separation where the nuclei are touching each other. In the control, the distance between the non-sister nuclei was ~25 µm. The color code is the same as in **F**.

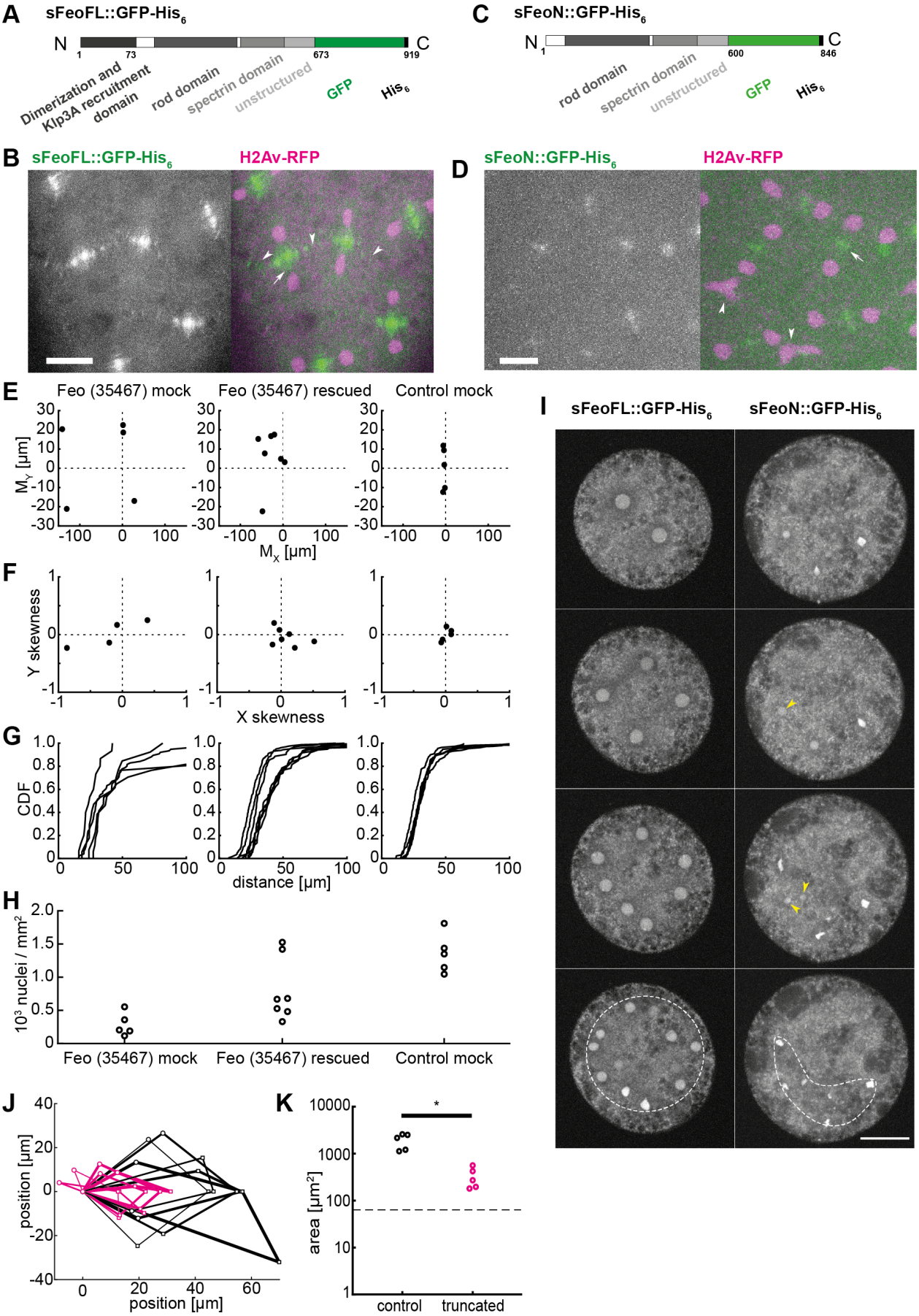
A
sFeoFL::GFP-His6
N
C
1
73
673
919
Dimerization and Klp3A recruitment domain
rod domain
spectrin domain
unstructured
GFP
His6
C
sFeoN::GFP-His6
N
C
1
600
846
rod domain
spectrin domain
unstructured
GFP
His6
B
sFeoFL::GFP-His6
H2Av-RFP
D
sFeoN::GFP-His6
H2Av-RFP
E
Feo (35467) mock
Feo (35467) rescued
Control mock
My [µm]
Mx [µm]
F
Y skewness
X skewness
G
CDF
distance [µm]
H
10³ nuclei / mm²
Feo (35467) mock
Feo (35467) rescued
Control mock
I
sFeoFL::GFP-His6
sFeoN::GFP-His6
J
position [µm]
position [µm]
K
area [µm²]
*
control
truncated

967

968

969 **Figure 5: Purified Feo protein rescues nuclear separation in Feo RNAi embryos, and a N-**
970 **terminally truncated Feo abolishes nuclear separation.**

971 **A)** Scheme of the synthesized full-length Feo protein fusion construct containing a C-terminal GFP.
972 The domains were determined based on sequence similarity from reported domains of the human
973 construct. The N-terminal end induces dimerization and binds Klp3A, and the spectrin domain
974 binds to microtubule lattice. **B)** Fluorescence image of the GFP-tagged full-length Feo protein in a
975 (control) blastoderm embryo in telophase after protein injection. The GFP signal alone (left) is
976 shown merged with H2Av::RFP in magenta (right). sFeoFL::GFP-His_6 localized correctly, under
977 cell cycle control, at the spindle midzone (arrow) and between daughter nuclei (arrowhead) as
978 observed in the transgenic overexpression fly line shown in Fig. 1. Scale bar, 10 µm. **C)** Scheme
979 of a truncated Feo construct lacking the first 73 amino acids of the putative dimerization and Klp3A
980 recruiting domain, fused to a C-terminal GFP. **D)** Fluorescence image of the GFP-tagged truncated
981 Feo protein in a (control) blastoderm embryo after protein injection. The GFP signal alone (left) is
982 shown merged with H2Av::RFP in magenta (right). A faint GFP signal localized at the spindle
983 midzone (arrow) in the second division after injection (Suppl. Fig. 4C). Nuclear separation defects
984 manifest as neighboring nuclei touching or fusing after division (arrowheads). Scale bar, 10 µm.
985 **E)** Plot of the 2-dimensional centroid vector (M_X,M_Y) of all cortical nuclei relative to the embryo
986 center for Feo RNAi embryos either mock injected (left; N=5) or injected with sFeoFL::GFP-His6
987 protein (middle; N=7), compared with mock injected control (mCherry) RNAi embryos (N=5).
988 The *x*-axis designates the anterior-posterior axis and the *y*-axis is the dorso-ventral axis of the
989 embryo. Deviations from zero mark an acentric delivery of nuclei to the cortex. Along the anterior-
990 posterior axis the injection of Feo full-length protein in Feo RNAi embryos partially rescued
991 centering (middle) while mock-injected Feo RNAi embryos had anatomically eccentric nuclei
992 (left), whereas mock-injected control (mCherry) RNAi embryos exhibited strong centering. **F)**
993 Skewness plot of the positional distribution of all nuclei along the anterior-posterior (*x*) and
994 dorsoventral (*y*) axis for the same conditions as in E. The asymmetric distribution in mock-injected
995 Feo RNAi embryos (left) is partially rescued by Feo protein injection (middle) while mock-injected
996 control embryos show little asymmetry. **G)** Cumulative distribution plot of the first-order neighbor
997 distance between nuclei, for the same conditions as in e) and f). The irregular internuclear distances
998 in mock-injected Feo RNAi embryos (left) are rescued to a considerable extent after full-length
999 protein injection (middle) while mock-injected control (mCherry) RNAi embryos exhibit uniform
1000 inter-nuclear distances (right). **H)** The low nuclear density arriving at the cortex in mock-injected
1001 Feo RNAi embryos is partially rescued when full-length Feo protein is injected in preblastoderm
1002 Feo RNAi embryos. **I)** Addition of full-length Feo::GFP protein to embryo explants supports
1003 normal nuclear division and regular distribution within the explant space (left, white circle) while
1004 addition of truncated Feo protein reduces nuclear separation (arrowheads) causing occasional
1005 spindle fusion, and abolishes nuclear distribution (dashed envelope). Scale bar, 30 µm. **J)** Overlay
1006 of aligned quadrilaterals describing the nuclear separation after division in explants, as described
1007 in Fig. 4. Explants were generated from wildtype embryos and had ample space for the first few
1008 divisions. Experiments involving addition of full-length GFP-tagged Feo protein to the explant are
1009 in black (N=5), experiments involving addition of N-terminally truncated, GFP-tagged Feo protein
1010 are shown in magenta (N=5). **K)** The truncated Feo protein significantly reduced nuclear

1011 separation, as measured by the area of quadrilaterals shown in **J**, as compared to the full-length
1012 protein construct (black).

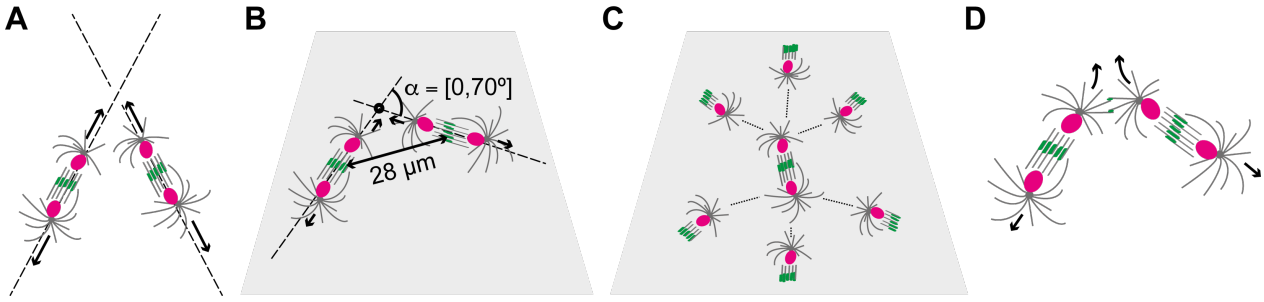

Figure 6: Feo and Klp3A prevent collision trajectories of dividing nuclei in space and on 2-dimensional topologies.

A) Two neighboring spindles with division axes that are oblique. Nuclei separate along the spindle axis, which do not have an intersecting point and do not cause nuclear collision. **B)** Two neighboring spindles with coplanar spindle axes. If these axes are not parallel, they will always form an intersection point. However, because of the short nuclear migration from the previous spindle center (~14 µm), the nuclear diameter (~5 µm) and the average inter-spindle distance (~28 µm), two non-sibling nuclei will only collide if the relative angle α between spindle axes is ≤70º. **C)** In a two-dimensional topology of spindles with optimal packing each spindle has six neighbors. In this configuration, and considering the geometric constraints shown in **B**, any orientation of spindle axis for the spindle in the center will lead to collisions with non-sibling nuclei. **D)** Model of aster mediated repulsion between neighboring nuclei on a colliding trajectory after mitosis. Astral microtubule crosslinking by Feo and Klp3A generates a repulsive mechanical element that deviates the direction of separating nuclei from the spindle axis.

1028 **Supplementary Figures**

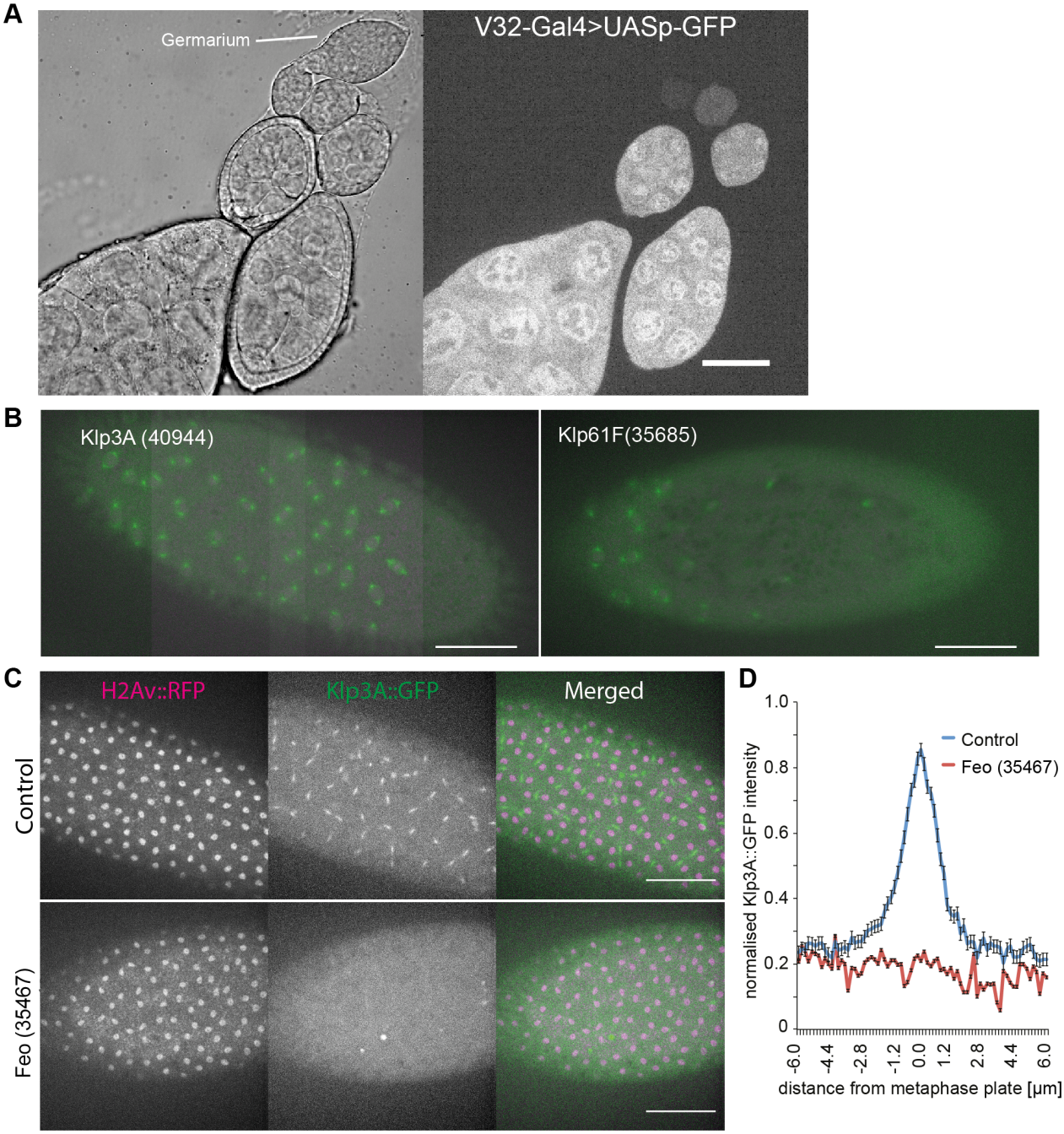

1029

1030 **Supplementary Figure 1 related to Figure 2: A) V32-Gal4 drives expression during late**
1031 **oogenesis.** A construct expressing V32–Gal4 driving UASp–GFP expression specifically in the
1032 female germline indicates that the peak expression of GFP is achieved only at late stages of
1033 oogenesis. It illustrates the expression pattern of UASp constructs under the same Gal4 driver,
1034 including the various RNAi constructs described here have maximum effect in late oogenesis. Scale
1035 bar, 10 µm. **B) Partial knockdown of Klp3A (40944) or Klp61F (33685) by RNAi leads to**
1036 **defective nuclear delivery to the embryo cortex.** Maximum intensity projections from three-
1037 dimensional time-lapse movies of embryos partially depleted of Klp3A or Klp61F, expressing
1038 Jupiter::GFP (green) marking microtubules and H2Av::RFP (magenta) marking chromatin. These
1039 two complementary RNAi lines showed that knockdown embryos exhibited irregular nuclear

1040 distribution during the first interphase occurring at the cortex as compared to the regular nuclear
1041 distribution in control embryos (RNAi against mCherry; Fig. 3A). Scale bar, 50 µm. **C-D) Partial**
1042 **depletion of Feo fails to recruit Klp3A to the spindle midzone. C)** Snapshots from a time-lapse
1043 of embryos expressing H2Av::RFP (magenta, left panel) and Klp3A::GFP (green, middle panel)
1044 during anaphase B or telophase. Feo knockdown embryos failed to recruit Klp3A at the spindle
1045 midzone when compared with the control embryos expressing no *feo* RNAi. **D)** Quantification of
1046 Klp3A::GFP intensity measured at the spindle midzone along the spindle axis in control and Feo
1047 RNAi (35467) embryos. Scale bar, 50 µm.

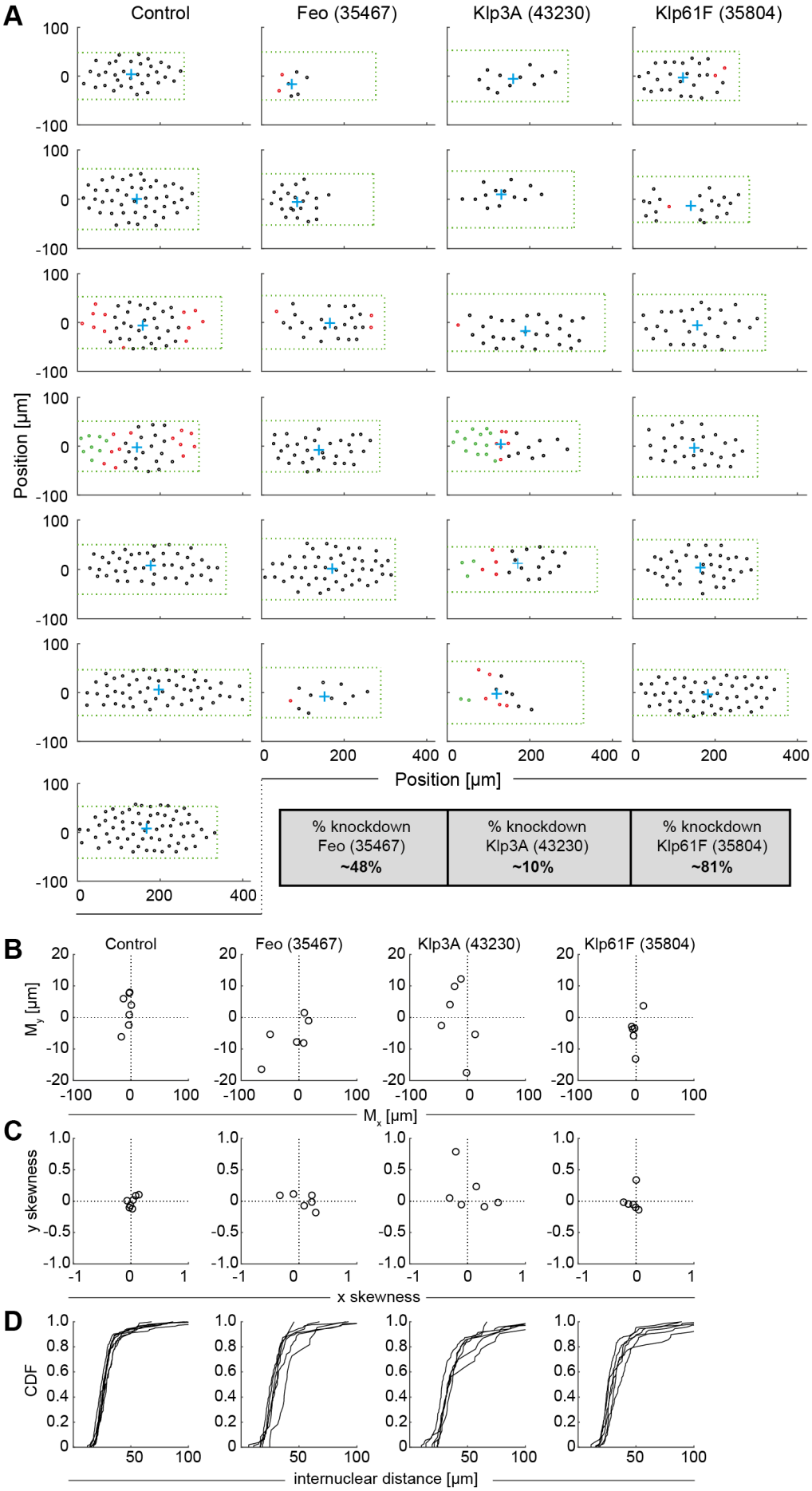
A
Control
Feo (35467)
Klp3A (43230)
Klp61F (35804)
Position [µm]
Position [µm]
% knockdown Feo (35467) ~48%
% knockdown Klp3A (43230) ~10%
% knockdown Klp61F (35804) ~81%
B
Control
Feo (35467)
Klp3A (43230)
Klp61F (35804)
M_y [µm]
M_x [µm]
C
y skewness
x skewness
D
CDF
internuclear distance [µm]

1048

1049 **Supplementary Figure 2 related to Figure 2: Positions of nuclei in each of the analyzed**
1050 **embryos and distribution measurements highlight irregularity in the knockdown constructs.**

1051 **A)** The position (circle) of every nucleus arriving at the embryo cortex after the last preblastoderm
1052 division, relative to the axial and lateral borders of the embryo, for each condition – Control
1053 (mCherry), Feo (35467), Klp3A (40320), Klp61F (35804). The green dashed rectangle represents
1054 the area of the embryo bounded by the length and width of the visible embryo in the confocal
1055 stacks, with the anterior end at the coordinate origin. The blue cross represents the location of the
1056 2-dimensional centroid determined from the position of all nuclei. The nuclei in interphase of the
1057 first division at the cortex are marked in black, the nuclei that have progressed to metaphase /
1058 anaphase are marked in magenta, and the nuclei in telophase / (next) interphase are marked in
1059 green. The percent knockdown of mRNA of the lines Feo (35467), Klp3A (40320) and Klp61F
1060 (35804) was 48%, 10% and 81%, respectively, as measured by quantitative PCR. **B)** Plot of the 2-
1061 dimensional centroid vector (M_x,M_y) of all cortical nuclei relative to the embryo center. The *x*-axis
1062 designates the anterior-posterior axis and the *y*-axis is the dorsoventral axis of the embryo.
1063 Deviations from zero mark an acentric delivery of nuclei to the cortex. **C)** Skewness plot of the
1064 positional distribution of all nuclei along the anterior-posterior (*x*) and dorsoventral (*y*) axis. Feo
1065 RNAi and Klp3A RNAi embryos showed asymmetric nuclear distribution while nuclei in Klp61F
1066 RNAi embryos were distributed symmetrically. **D)** Cumulative distribution plot of the first-order
1067 neighbor distance between nuclei. All RNAi lines showed higher variability in internuclear
1068 distance as compared with the control.

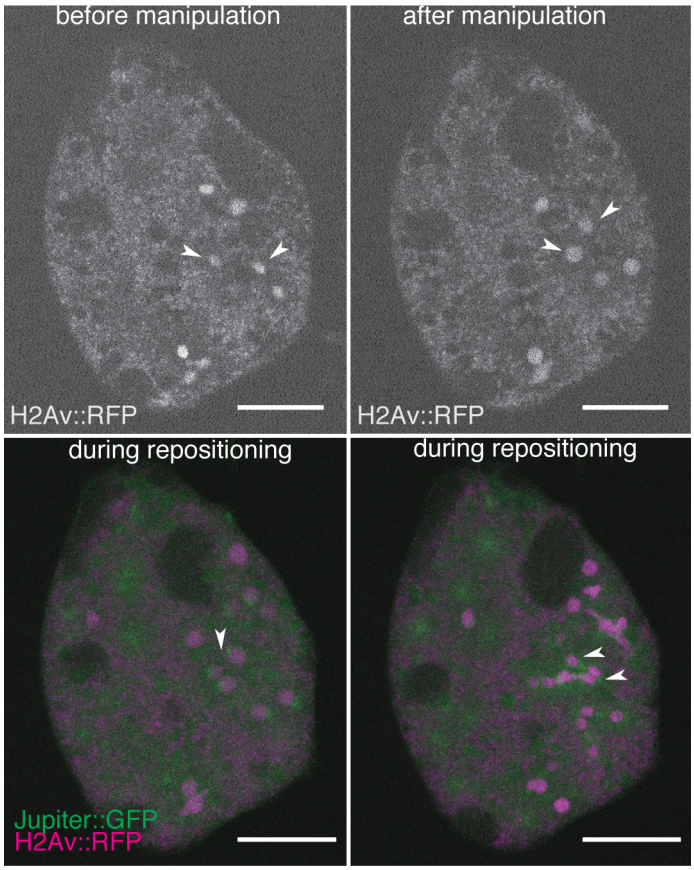

Supplementary Figure 3 related to Figure 4: Partial depletion of Feo fails to maintain nuclear separation after manipulation.

Physical manipulation of nuclear position in an explant made from an embryo depleted of Feo and expressing Jupiter::GFP (green) marking microtubules and H2Av::RFP (magenta) marking chromatin. After manipulation, the nuclei failed to elicit an efficient repositioning response as observed in the control (Fig. 4). Instead, sister and non-sister nuclei failed to separate sufficiently, and nuclei came into contact or formed clusters. Scale bar, 30 µm.

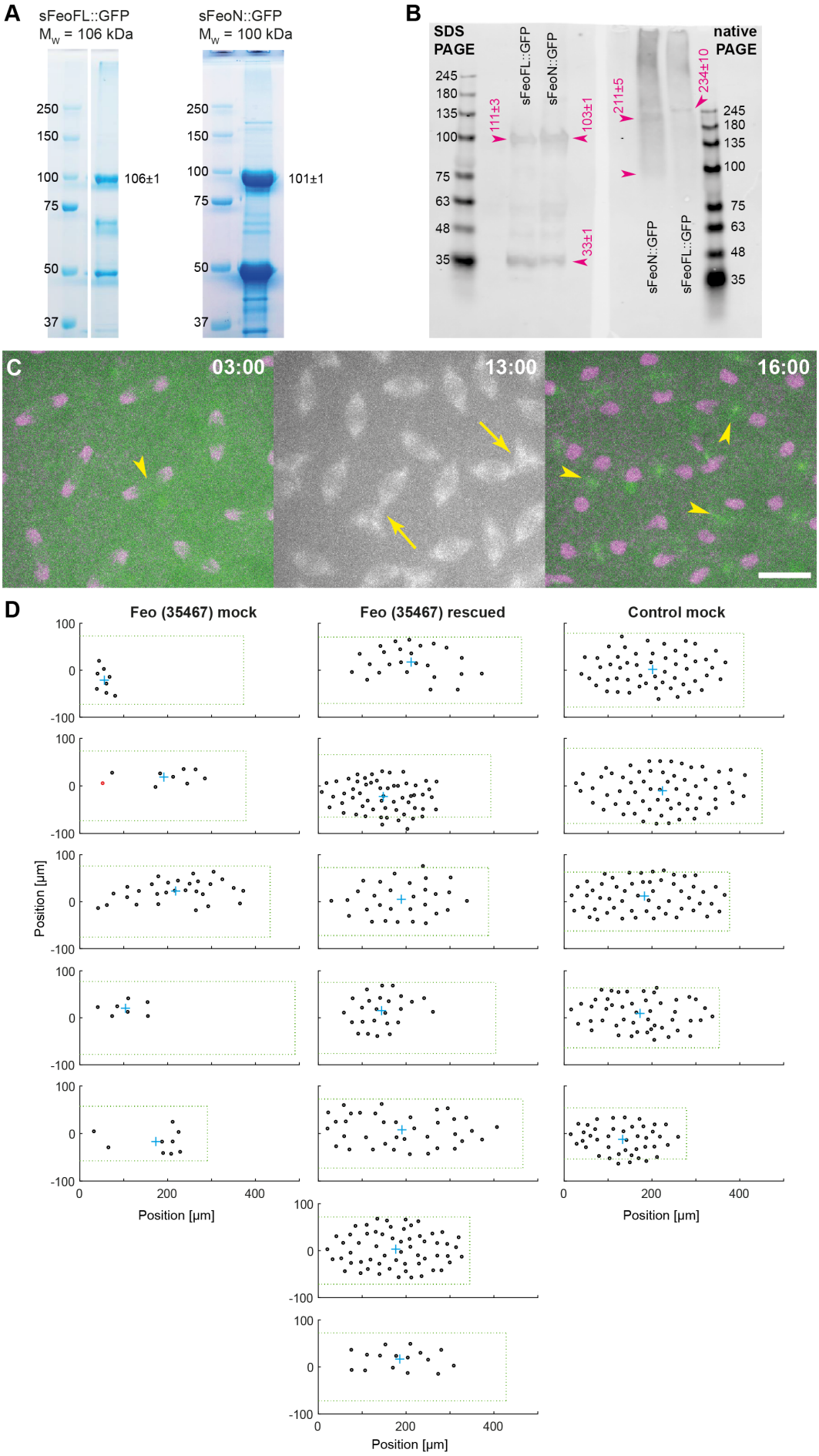
A
sFeoFL::GFP
M_w = 106 kDa
sFeoN::GFP
M_w = 100 kDa
250
150
100
75
50
37
106±1
101±1
B
SDS PAGE
native PAGE
245
180
135
100
75
63
48
35
111±3
103±1
33±1
211±5
234±10
sFeoFL::GFP
sFeoN::GFP
C
03:00
13:00
16:00
D
Feo (35467) mock
Feo (35467) rescued
Control mock
Position [µm]
100
0
-100
0
200
400

1077

1078 **Supplementary Figure 4 related to Figure 5: N-terminally truncated Feo::GFP weakly**
1079 **dimerizes and causes nuclear separation defects, and full-length Feo::GFP protein partially**
1080 **rescues nuclear delivery to the cortex of Feo RNAi embryos.**

1081 **A)** Coomassie-stained 15% SDS PAGE of heterologous expressed and purified full-length
1082 Feo::GFP (left) and an N-terminally truncated Feo::GFP construct missing the putative
1083 dimerization and Klp3A-binding domain. The expected molecular mass is at the top, the measured
1084 mass is on the right of the bands (details in Methods). The lower bands are contaminants that were
1085 not separated by gel filtration and are of bacterial origin as determined by mass spectrometry. **B)**
1086 Western blot of a 4-12% gradient SDS PAGE (left) next to a Native-PAGE (right) with FeoFL:GFP
1087 and FeoN:GFP, using mouse anti-GFP antibody. Both protein constructs migrate according to
1088 expected molecular mass of a monomer in the SDS PAGE gel. In the Native-PAGE gel the full-
1089 length Feo migrates as expected from a dimer. The slight deviation from the expected mass of a
1090 dimer (212 kDa) can be explained by the rod-like structure of the protein, as was shown for the
1091 human homolog PRC1 [Subramanian et al 2010]. Conversely, the truncated construct migrates like
1092 a weak dimer, causing a wide distribution ranging between 100–200 kDa. **C)** Time-lapse
1093 fluorescence images of a (control) blastoderm embryo expressing H2Av::RFP (magenta) after
1094 injection of FeoN::GFP protein (green) and Alexa647-Tubulin (grey). During the cycle just after
1095 injection (left), the localization of FeoN::GFP at the spindle midzone was not detectable
1096 (arrowhead). However, the effect of protein addition manifests in nuclear separation defects, and
1097 in the subsequent division (middle) spindles are observed in unnatural proximity leading to spindle
1098 fusion (arrow). In telophase of the same cycle (right) FeoN::GFP is detected at the spindle midzone
1099 (arrowheads). This delayed localization after injection is not observed for FeoFL::GFP (Fig. 5B)
1100 and indicates that dimerization of Feo could be dynamic, cell-cycle dependent and, consequently,
1101 heterodimers of endogenous and truncated Feo are formed. Time is in min:sc. Scale bar, 10 µm.
1102 **D)** The position (circle) of every nucleus arriving at the embryo cortex after the last preblastoderm
1103 division, relative to the axial and lateral borders of the embryo, for each condition: Feo (35467)
1104 mock-injected (buffer), Feo (35467) rescued by protein injection, Control (mCherry) mock-
1105 injected. The green dashed rectangle represents the area of the embryo bounded by the length and
1106 width of the visible embryo in the confocal stacks, with the anterior end at the coordinate origin.
1107 The cyan cross represents the location of the 2-dimensional centroid defined from the position of
1108 all nuclei. The nuclei in interphase of the first division at the cortex are marked in black, nuclei that
1109 have progressed to metaphase / anaphase are marked in magenta.

1110

Supplementary Videos

Suppl. Video 1: Maximum intensity Z-projection from a 3D time-lapse movie of an explant generated from an embryo expressing Klp61F::GFP (cyan), Feo::mCherry (green) and injected with Alexa647-Tubulin (magenta). Time in h:min:ss, scale bar 30 µm, frame rate is 7 min^{-1}. In support of Fig. 1.

Suppl. Video 2: Maximum intensity Z-projection from a 3D time-lapse movie of an embryo expressing Klp61F::GFP (cyan), Feo::mCherry (green) and injected with Alexa647-Tubulin (magenta). Time in h:min:ss, scale bar 10 µm, frame rate is 7 min^{-1}. In support of Fig. 1.

Suppl. Video 3: Maximum intensity Z-projection from a 3D time-lapse movie of an embryo expressing Klp3A::GFP (cyan), Feo::mCherry (green) and injected with Alexa647-Tubulin (blue). Time in h:min:sec, scale bar 10 µm, frame rate is 7 min^{-1}. In support of Fig. 1.

Suppl. Video 4: Maximum intensity Z-projection from four 3D time-lapse movies of embryos expressing Jupiter::GFP (green) and H2Av::RFP (magenta), expressing RNAi against mCherry (Control), Feo (35467), Klp3A (43230) and Klp61F (30804). Time in min:sec, scale bar 50 µm, frame rate is 7 min^{-1}. In support of Fig. 2.

Suppl. Video 5: Maximum intensity Z-projection from a 3D time-lapse movie of an embryo expressing H2Av::RFP (magenta) and injected with sFeoFL::GFP protein (green). Time in h:min:sec, scale bar 10 µm, frame rate is 7 min^{-1}. In support of Fig. 5.

Suppl. Video 6: Maximum intensity Z-projection from a 3D time-lapse movie of an embryo expressing Spd::GFP (green, marking centrosomes), Jupiter::mCherry (magenta) and injected with sFeoFL::GFP protein (green). Time in h:min:sec, scale bar 10 µm, frame rate is 7 min^{-1}. In support of Fig. 5.

Suppl. Video 7: Maximum intensity Z-projection from a 3D time-lapse movie of an embryo expressing RFP::β-Tubulin (magenta) and injected with sFeoN::GFP (green) and Alexa647-Tubulin (grey). The merge shows the GFP and RFP only. Time in h:min:sec, scale bar 30 µm, Frame rate is 7 min^{-1}. In support of Fig. 5.